Experimental Evaluation of P-Y Curves Considering Liquefaction Development

WA-RD 762.1

Barbara Chang
Tara C. Hutchinson

December 2010

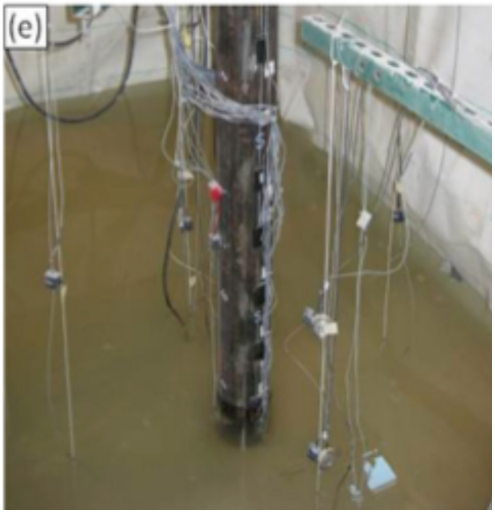

Washington State Department of Transportation
Office of Research & Library Services

WSDOT Research Report

EXPERIMENTAL EVALUATION OF P-Y CURVES CONSIDERING LIQUEFACTION DEVELOPMENT

Final Report

by
Barbara Chang
Tara C. Hutchinson

Department of Structural Engineering
University of California, San Diego

Prepared for

Washington State Department of Transportation
Paula J. Hammond, Secretary
Olympia, WA 98504-7372

December 2010

Columbia River CROSSING

TECHNICAL REPORT STANDARD TITLE PAGE

1. REPORT NO.	2. GOVERNMENT ACCESSION NO.	3. RECIPIENT'S CATALOG NO.
WA-**RD 762.1**		

4. TITLE AND SUBTITLE	5. REPORT DATE
Experimental Evaluation of P-Y Curves Considering Liquefaction Development	**December 2010**
	6. PERFORMING ORGANIZATION CODE

7. AUTHOR(S)	8. PERFORMING ORGANIZATION REPORT NO.
Barbara Chang and Tara C. Hutchinson	

9. PERFORMING ORGANIZATION NAME AND ADDRESS	10. WORK UNIT NO.
University of California, San Diego **Department of Structural Engineering** **La Jolla, CA 92093-7436**	11. CONTRACT OR GRANT NO. **GCA 5977**

12. SPONSORING AGENCY NAME AND ADDRESS	13. TYPE OF REPORT AND PERIOD COVERED
Research Office Washington State Department of Transportation Transportation Building, MS 47372 Olympia, Washington 98504-7372 Research Manager: Kim Willoughby 360.705.7978	**Research Report**
	14. SPONSORING AGENCY CODE

15. SUPPLEMENTARY NOTES

This study was conducted in cooperation with the U.S. Department of Transportation, Federal Highway Administration.

16. ABSTRACT:

This report presents details and findings of a test series conducted on a single pile embedded in homogeneous saturated Nevada sand, which was subjected to sequential dynamic shaking and lateral (inertial-equivalent) loading. This report documents the model test design and construction, details regarding the loading protocol, test observations and post test results. A key goal in the test program was to develop a data set capable of rendering insight into the characteristics of 'p-y' resistance under developing liquefied soil conditions. While evidence in the literature indicates that this resistance is reduced as excess pore pressure increases, the shape and amplitude of how the reduced p-y curve develops during pore pressure build-up are needed for reliable design of pile foundations in areas prone to earthquake-induced soil liquefaction. Analyses of the experimental data show that mobilization of the partially liquefied soil was achieved during lateral loading. Additional data was evaluated including wave test measurements (hammer strikes to model), settlement, and acceleration measurements. Results presented focus importantly on the static p-y curves back-calculated from the bending moment distributions at the achieved excess pore pressures. A rich set of test data was produced from this testing series, which will be useful for model validation and subsequent design efforts.

17. KEY WORDS	18. DISTRIBUTION STATEMENT
Liquefaction, p-y curve, piles, soil	No restrictions. This document is available to the public through the National Technical Information Service, Springfield, VA 22616

19. SECURITY CLASSIF. (of this report)	20. SECURITY CLASSIF. (of this page)	21. NO. OF PAGES	22. PRICE
None	None		

Title VI

The Columbia River Crossing project team ensures full compliance with Title VI of the Civil Rights Act of 1964 by prohibiting discrimination against any person on the basis of race, color, national origin or sex in the provision of benefits and services resulting from its federally assisted programs and activities. For questions regarding WSDOT's Title VI Program, you may contact the Department's Title VI Coordinator at (360) 705-7098. For questions regarding ODOT's Title VI Program, you may contact the Department's Civil Rights Office at (503) 986-4350.

Americans with Disabilities Act (ADA) Information

If you would like copies of this document in an alternative format, please call the Columbia River Crossing (CRC) project office at (360) 737-2726 or (503) 256-2726. Persons who are deaf or hard of hearing may contact the CRC project through the Telecommunications Relay Service by dialing 7-1-1.

¿Habla usted español? La informacion en esta publicación se puede traducir para usted. Para solicitar los servicios de traducción favor de llamar al (503) 731-4128.

Disclaimer

The contents of this report reflect the views of the authors, who are responsible for the facts and accuracy of the data presented herein. The contents do not necessarily reflect the official views or policies of the Washington State Department of Transportation or the Federal Highway Administration. This report does not constitute a standard, specification, or regulation.

TABLE OF CONTENTS

List of Figures

List of Tables

Appendices

ACRONYMS

ADA	Americans with Disabilities Act
API	American Petroleum Institute
CISS	cast-in-steel-shell
CRC	Columbia River Crossing
ODOT	Oregon Department of Transportation
UCSD	University of California, San Diego
WSDOT	Washington State Department of Transportation

This page left blank intentionally.

Executive Summary

This report presents details and findings of a test series conducted on a single pile embedded in homogeneous saturated Nevada sand, which was subjected to sequential dynamic shaking and lateral (inertial-equivalent) loading. This report documents the model test design and construction, details regarding the loading protocol, test observations and post test results. Experiments were conducted at the University of California, San Diego, Powell Laboratories. A key goal in the test program was to develop a data set capable of rendering insight into the characteristics of 'p-y' resistance under developing liquefied soil conditions. While evidence in the literature indicates that this resistance is reduced as excess pore pressure increases, the shape and amplitude of how the reduced p-y curve develops during pore pressure build-up are needed for reliable design of pile foundations in areas prone to earthquake-induced soil liquefaction. Recent research has shown that the shape of the p-y resistance curves during liquefaction of the soil is not merely a reduction of the soil resistance in stable soil but rather may manifest an inverted S-shaped behavior, which has low (or zero) soil resistance at low displacement and stiffens at larger displacements.

Analyses of the experimental data show that mobilization of the partially liquefied soil was achieved during lateral loading. Additional data was evaluated including wave test measurements (hammer strikes to model), settlement, and acceleration measurements. Results presented focus importantly on the static p-y curves back-calculated from the bending moment distributions at the achieved excess pore pressures. A rich set of test data was produced from this testing series, which will be useful for model validation and subsequent design efforts.

This page left blank intentionally.

1. Introduction

1.1 Problem Statement

Upon liquefaction, the strength and stiffness of the surrounding soil dramatically decreases. Consistent with this observation, the soil resistance in terms of strength and stiffness provided to a laterally loaded pile foundation, conventionally modeled with non-linear p-y curves, is also reduced. The underlying p-y curve that is reduced has typically been back-calculated from pile load tests conducted in stable ground (not liquefied) and modified with a scalar factor applied independently to strength and stiffness. However, it is unclear how the shape and amplitude of the reduced p-y curve develops during various levels of excess pore pressure. The characteristics of the change in soil resistance during the development of excess pore pressure are needed for reliable design of pile foundations in areas prone to earthquake-induced soil liquefaction.

1.2 Related Work

Efforts to characterize the resistance of soil imposed on a pile subjected to lateral loading can be traced back to the 1930s (Feagin, 1937). In this study, Feagin (1937) tested timber and concrete piles embedded in saturated Mississippi river sand under lateral loading. Single free-head piles and fixed head pile groups of four, twelve, and twenty were tested with cyclic and monotonic loading. By comparing load versus deflection plots of piles-absent-soil and piles-in-soil, Feagin concludes that passive pressure of the soil provides a significant portion of the resistance to lateral movement of the pile, except in the near surface portion of the soil where structural rigidity of the pile was of greater importance.

Many years later, Reese et al. (1974) conducted lateral load tests on two full-sized 24" diameter piles, which were driven into layers of clean fine sand to silty fine sand on Mustang Island near Corpus Christi, Texas. The water table was maintained above ground during testing. Static and cyclic lateral loads were applied to the piles. Piles were instrumented for measuring bending moments along the length of the pile, and from the experimental bending moment profiles along the pile, soil resistance p and displacement y at points on the pile were obtained via integration and differentiation. Displacement y was obtained by double integrating the moment divided by EI with respect to the length of the pile, and soil resistance p was obtained by double differentiating the bending moment (with appropriate boundary conditions) with respect to the length of the pile. When a comparison of the predicted computed values of the ultimate soil resistance was made with the measured values, it was found that agreement was “poor.” An empirical adjustment factor was used to reconcile the difference in values. These and other classical test programs form the basis for many p-y resistance curves used readily in practice today [e.g. Matlock (1970); API (1993)].

In recognition of the high likelihood that piles may be used in zones of high seismicity and are often placed in soil conditions prone to liquefaction, a concerted effort has been undertaken to investigate the soil resistance characteristics where soil liquefies. Experimental efforts have been undertaken at both the centrifuge and 1-g scales. For example, centrifuge tests include those of

Liu and Dobry (1995); Wilson et al. (2000), and Brandenberg et al. (2005), to name a few. Relevant full-scale tests include laterally loaded piles during blast-induced liquefaction [Weaver et al. (2005) and Rollins et al. (2005, 2007)], as well as 1-g shake table tests (e.g. Meymand (1998); Tokimatsu and Suzuki (2004); Tokimatsu et al. (2001)). In the following paragraphs, a cursory review of important related research efforts is provided.

Centrifuge modeling of piles and their lateral soil resistance during liquefaction was conducted by Liu and Dobry (1995) at the geotechnical centrifuge facility at Rensselaer Polytechnic Institute. A single fixed-base model brass pile was tested in a homogeneous layer of #120 Nevada sand (D_r = 60%), which was saturated with a de-aired water-glycerol mixture for the pore fluid. The pile head was locked in place during spin-up of the centrifuge while dynamic ground motion was input from the base of the box. Immediately after the dynamic shake, the pile head was unlocked, and a cyclic static lateral load was applied. Rotation of the pile head was prevented during static loading. P-y curves were back-calculated using measured bending moments. A simple analysis with the software program LPILE (Reese et al., 2000) was conducted with these p-y curves, and the predicted bending moments of the pile corresponded well with the experimental data. Liu and Dobry concluded that the lateral resistance of the liquefied soil may be represented by a scalar multiple of its static drained lateral resistance despite undrained load conditions.

Wilson et al. (2000), with more detail provided in Wilson (1998), also studied the effect of liquefaction on the soil resistance for laterally loaded piles using centrifuge testing at the University of California, Davis. A series of tests was performed on single piles and pile groups. The piles were tested in a two-layer soil profile with the base of the single pile embedded in a bottom layer of dense sand of about 80% relative density. Two different upper layer soil conditions were constructed, specifically a loose sand (D_r = 35%) and a medium-dense sand (D_r = 55%). The sand was saturated with a de-aired water-glycerol mixture for the pore fluid. The pile-soil model was subjected to earthquake ground motion, and its p-y behavior during liquefaction was back-calculated. The back-calculated p-y curves were smaller and softer for the 35% relative density specimen than for the specimen at 55% relative density. Progressive softening of the p-y curves during shaking events was also observed for increasing excess pore pressure, soil strains, and number of cycles. Softening was attributed to the soil's memory of larger prior relative displacements. Increased soil resistance that developed during strong shaking is attributed to phase transformation and deliquefaction of the saturated sand. Additionally, a hardening response was observed as an inverted S-shape when lateral displacements approached and exceeded maximum past displacements during the shaking event [Figure 1-1(a)]. Wilson (1998) suggests a scalar reduction multiplier for the p-y curve (applied to both strength and stiffness) of 0.25 to 0.35 for relative densities equal to 55% and of 0.10 for relative density equal to 35%.

Tests by Brandenberg et al. (2005), with more detail provided in Brandenberg (2005), examined the response of eight dynamic model tests of single piles and pile groups also at the University of California, Davis, centrifuge. Prototype pile diameters were 0.36 to 1.45 meters for single piles and 0.73 to 1.17 meters for pile groups. The soil profile was a gently sloping non-liquefied crust on top of a liquefiable loose sand over dense sand. Earthquake ground motions were input to the base of the soil box with peak base accelerations ranging from 0.13g to 1.00g. During shaking, several transient drops in pore pressure in the loose sand were attributed to undrained shear

loading of the dilatant soil. The transient drops in pore pressure were attributed to dilatancy instead of drainage because the rate of post-shaking pore pressure dissipation was too slow to affect pore pressures during an individual cycle of shaking. Brandenberg (2005) recommends p-multiplier values of 0 to 0.5 based on corresponding $(N_1)_{60-CS}$ values of less than 8 blows to more than 24 blows of the soil for static-seismic analysis of pile foundations. The value of p_u (ultimate soil strength) was assumed to vary linearly for r_u = 0% to r_u = 100%.

Back-calculated p-y curves were also studied in a full-scale test of laterally loaded piles during blast-induced liquefaction (Weaver et al., 2005; Weaver, 2001). Full-scale blast-induced liquefaction lateral load tests on a 0.6 meter and a 0.9 meter diameter cast-in-steel-shell (CISS) pile were conducted at Treasure Island, a manmade island constructed in the 1930s for the Golden Gate International Expansion. The island was constructed via hydraulic filling dredged material from the Sacramento River over the shoals of neighboring Yerba Buena Island. The soil is relatively loose and prone to liquefaction, which occurred at this site during the 1989 Loma Prieta earthquake. The soil profile includes Bay Mud overlaid by loose, saturated sand with intermittent clay zones, which is overlaid by medium dense sand near the surface. Ground water was at a depth of 1.9 meters. Inertial loading was simulated by using hydraulic actuators at the pile head applied in a cyclic load pattern. Lateral loads were applied to the CISS pile before and after detonation of the below-ground explosives. As an indication of liquefaction, excess pore pressure ratios varied between 70% to 100% immediately around the pile and 30-90% at a distance of 4.2 meters from the pile. Visual evidence of liquefaction was apparent from sand boils at the ground surface some minutes after blasting. Due to blast liquefaction, the liquefaction process of the soil was initiated deep in the soil profile rather than at the surface. The back-calculated p-y curves presented an initially flat p-y curve, which only stiffened upon increasing displacement [Figure 1-1(b)]. The liquefied soil resistance exceeded that of the static soil resistance and showed no indication of yielding. The shapes of these liquefaction p-y curves are significantly different from conventional p-y curves. No soil resistance to lateral pile movement is observed until to 50mm (approximately 8% of pile diameter) was observed. At large displacements, an increase in lateral soil resistance occurred which may have been caused by phase transformation of the sand which in turn caused a reduction of pore water pressure and thus increased soil lateral resistance.

Blast-induced liquefaction pile tests were also conducted by Rollins et al. (2005, 2007) at the Ravenel bridge site in Charleston, South Carolina. Lateral load tests were performed on a 2.59m diameter CISS drilled shaft pile foundation before and after blast-induced liquefaction. The pile was embedded in alluvial sands and sandy clay layers to a depth of 13 to 14 meters; beneath these layers was a stiff clay layer. Depending on tidal fluctuation, the water table was located between the ground surface and 1.5 meters below the ground surface. The charges were detonated from the bottom upwards in a ring around the pile. By controlled blasting, the soil was liquefied to a depth of 13m. Excess pore pressure ratios of 80% to 100% were obtained. Lower r_u values occurred in the sandy clay layer (2 to 3 meters below the ground surface). A hydraulic load actuator and a statnamic loading device were used to apply the lateral load to the CISS pile foundation. An empirically derived equation for the p-y response of fully liquefied sand was developed for sands with relative density of 50% (Rollins et al., 2005):

$$p = A(By)^C p_d \tag{1.1}$$

where p = lateral soil pressure per length of the pile (kN/m), y = horizontal pile deflection (mm), $A = 3\times10^{-7}\times(z+1)^{6.05}$, $B = 2.80\times(z+1)^{0.11}$, $C = 2.85\times(z+1)^{-0.41}$, z = depth in meters, and $p_d = 3.81\times In(d)+5.6$, where d is the pile diameter in meters. Using this equation for p-y curves for the pile (with $p_d = 9.0$), the computed load-deflection curve agreed well with the measured curve from the experiment. Rollins et al. conclude that p-y curves for sands of less than relative density of 35% may be assumed flatter, and p-y curves of relative density greater than 50% may be assumed stiffer than those predicted by equation 1.1.

Although the reduction of soil stiffness and strength of laterally loaded piles during liquefaction is substantiated by past research, it is not clear whether the inverted S-shape initiates at a particular r_u value, and if so, at what value. The inverted S-shaped p-y curve indicates low (or zero) soil resistance at low displacements, while subsequently presenting stiffening at larger displacements. Liquefaction of the saturated soil is responsible for the change in p-y behavior, but the degree of excess pore water pressure to achieve the S-shaped p-y curve is unknown [Figure 1-1(c)]. It is speculated that at some point between a soil's stable state and liquefaction, the bilinear shaped p-y curve behavior may invert. The stages leading up to complete liquefaction, has not been studied thoroughly enough to determine the developing characteristics of partially liquefied soil p-y behavior.

Figure 1-1. Comparison of p-y curves in stable and liquefied soil

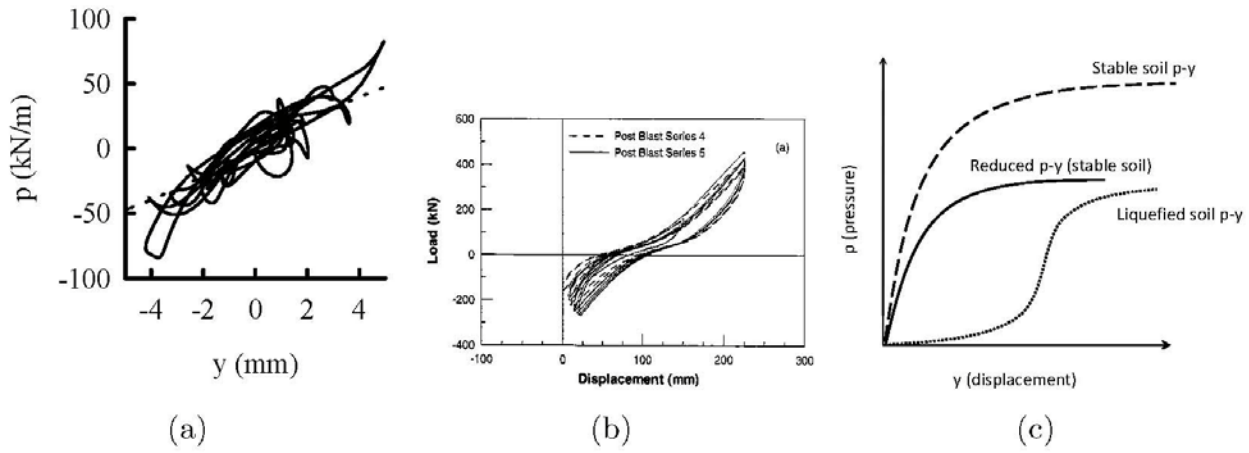

Figure 1-1: (a) sample p-y curve in liquefied soil (Wilson, 1998), (b) sample p-y curve in liquefied soil (Weaver, 2001), and (c) schematic of p-y curves with stable soil (API, 1993) and liquefied soil.

1.3 Scope

The objective of this project is to experimentally determine nonlinear p-y curves at various levels of liquefaction, as characterized by a range of earthquake-induced excess pore pressure ratios r_u. These experimentally developed curves will support computational modeling of soil-pile systems, including those needed for the design of the Columbia River Crossing (CRC). To address this objective, a single soil-pile experiment series was conducted at the University of California, San Diego (UCSD) in a large laminar soil box. The pile was instrumented along its length to capture its bending moment distribution. Dynamic base shaking was applied to the model to generate target excess pore pressure ratios. Upon development of excess pore pressures,

the intent was to laterally load the pile monotonically at its head to induce an inertial-equivalent response. Resistance at the soil-pile interface was evaluated by back-calculating the pressure-deformation relationship during each of the monotonic loading phases. Parallel cyclic simple shear tests were conducted on the sand used in these experiments. These simple shear tests were conducted by Shannon and Wilson, and thus not part of the scope of UCSD's efforts. In the chapters that follow, the experimental program, methods, and processed results are presented.

This page left blank intentionally.

2. Experimental Setup and Model Construction

2.1 Configuration

The test program was conducted using a large 1-g laminar soil box mounted on a uniaxial shake table (Figure 2-1 and Figure 2-2). The shake table has a platen footprint of 16' x 10', vertical load capacity of 80 kips, and lateral load capacity of 110 kips. The total displacement stroke of the dynamic actuator is 12 inches, and its maximum velocity is 35 inches per second.

Figure 2-1. Laminar soil box on shake table (elevation views)

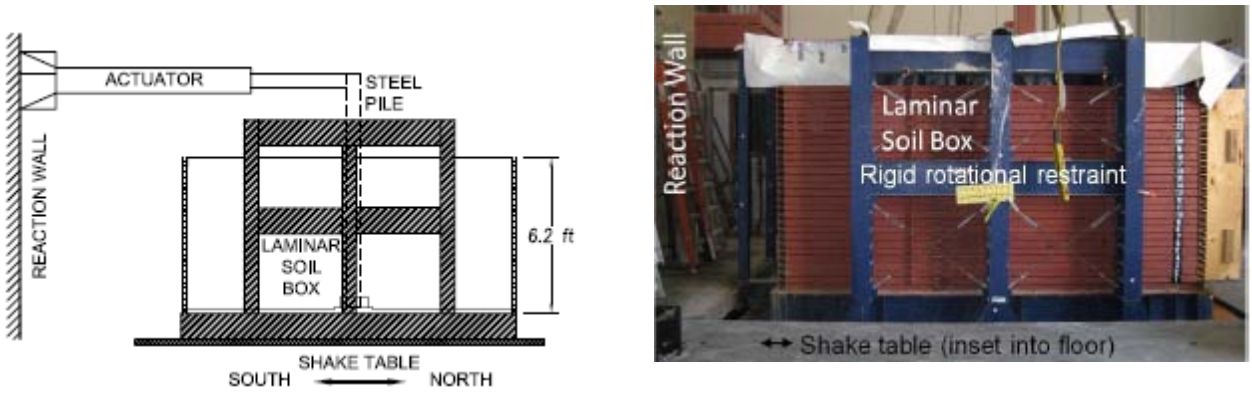

(a) (b)

Figure 2-1: (a) Schematic of laminar soil box on shake table and (b) photograph of laminar box on shake table (elevation views).

Figure 2-2. Laminar soil box on shake table (plan views)

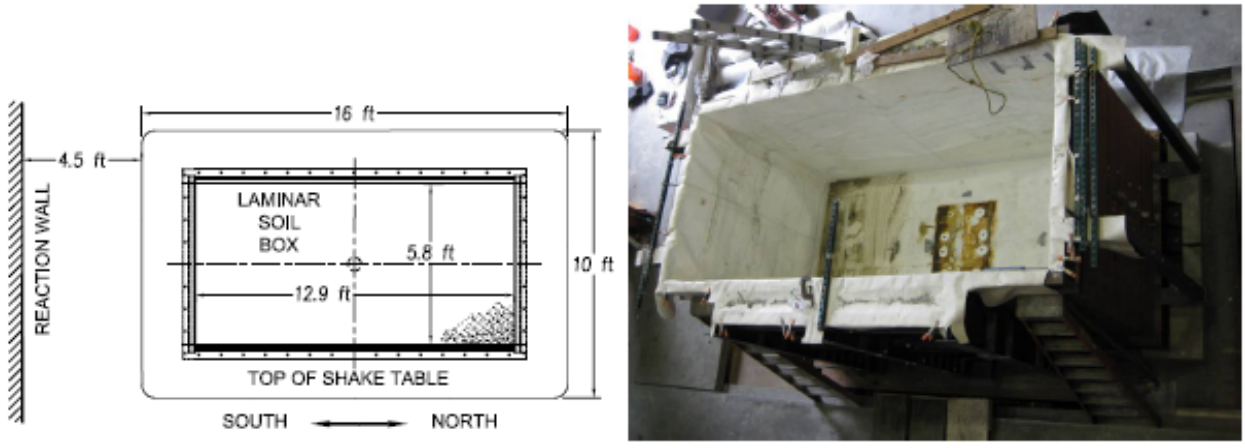

(a) (b)

Figure 2-2: (a)Schematic of laminar soil box on shake table and (b) photograph of laminar box on shake table (plan views).

The laminar soil box is comprised of 28 stacked frames with rollers sandwiched between the frames. Inside dimensions of the laminar soil box are 69.7" (W) x 154" (L) x 74.0" (H). A single steel tubular pile was placed vertically in the laminar soil box and surrounded by medium-loose saturated Nevada sand with a target relative density of D_r = 50%. The pile extends to the base of the box where it is connected with a collar assembly. The design and proof-testing of the laminar box are presented in Ashford and Jakrapiyanun (2001).

2.2 Soil Placement Trials

To achieve a homogeneous saturated soil layer of medium-loose density, wet sedimentation (air pluviation over a water head) was used to place the soil into the laminar soil box. Initial pluviation trials were conducted to determine the optimal parameters for placing the sand. Figure 2-3 shows the equipment that was used for the pluviation trials. The placement process was conducted as follows: A bag of kiln-dried sand was suspended over the hopper. This hopper has a series of specifically sized meshes at the beginning and at the end of the tube. Via this tube, the sand was dropped into the container, which contained a certain volume of still water. The sand grains fell from the end of the tube, which was positioned two inches above the water, and into the water. The sand grains subsided gently through the eight inches of water and then settled onto the bottom of the container. Sand grains were dropped into the water until a five inch thick lift was achieved. The volume of sand that was dropped into the container was measured, and the weight of the bag of sand was measured before and after pluviation. Sand was weighed using a heavy-duty scale with a maximum capacity of 10000 lbs. Using this data, the relative density of the saturated soil layer was estimated. After obtaining a reliable and reasonably close-to-target relative density from the pluviation trials (Table 2-1), this method was adopted for subsequent placement of the soil in the large laminar soil box.

Figure 2-3. Pluviation Trials

Figure 2-3: (a) pluviation equipment shown for placing sand in trial pluviation box and (b) sand fall from end of pluviation tube.

Table 2-1. Pluviation Trials with Nevada Sand #60

Trial #	Dropped Sand (lbs)	Volume (ft^3)	Dry density (pcf)	D_r (%)
1	325	3.178	102.3	42
2	688	6.701	102.6	45

2.3 Model Instrumentation

The saturated soil layer and the steel pile were heavily instrumented to monitor acceleration, load, pressure, strain, and displacements during the test program. Cameras were used to monitor the surface of the soil and elevation of the box and pile extension during shaking. Instruments were embedded in the saturated soil layer and placed around and outside of the laminar soil box (Figure 2-4 to Figure 2-8). In total, 93 channels of data acquisition were used in the test program. Sensitivities of the instruments are summarized in Table B.1 in the Appendix.

To install instruments that were embedded within the saturated soil layer, a steel Unistrut frame support system was clamped across the top of the laminar soil box. This steel frame support system was removed during testing. Instrument cables were secured to the Unistrut steel frame, and instruments were suspended in the empty prepluviation box at their approximate vertical and horizontal locations. Instruments were hot-glued to vertical steel strings attached to the steel frame support system with enough vertical slack between instruments so that embedded instruments would be free to move. The majority of these embedded soil instruments were placed along the centerline of the pile in the direction of loading. Two accelerometers were placed off the centerline on the east and west sides of the pile.

A total of five pore pressure transducers (Figure 2-4) were placed in a vertical arrangement near the pile and far from the pile in the soil column to monitor the buildup of excess pore pressure during dynamic shaking. In addition, one was placed near the bottom of the saturated layer at approximately 13" from the bottom of the box. Two more were placed near the middle of the saturated soil layer at approximately 39" up from the bottom. The last two were placed near the top of the saturated soil layer at approximately 5" below the ground surface.

Nine soil pressure sensors were distributed throughout the homogeneous soil layer. These soil pressure transducer measurements are unreliable during dynamic shaking as they record spurious pressures during acceleration. However, absolute differences in soil pressure at the beginning and the end of dynamic tests is reliable.

Seventeen accelerometers (Figure 2-7) were distributed in the homogeneous soil layer (A01 to A17). Two were placed at vertical instrument line A at 10D away from the face of the pile. Sensor A01 was placed near the top of the soil layer (initially 5" below ground surface), and A02 was placed near the middle of the soil layer (initially 39" up from the bottom of the soil layer). Another three accelerometers were placed at instrument line B at 6D away from the south face of the pile. These three accelerometers (A03, A04, and A05) were placed evenly spaced vertically within the soil. Ten accelerometers (A06 to A10; A13 to A17) were placed at instrument line C and D, respectively, to record the near-pile accelerations in the soil. These were also evenly spaced vertically within the soil layer.

Five accelerometers and two inclinometers were installed on the pile [Figure 2-6(a)] to measure acceleration during the shaking and pre-and-post shaking rotation. Fifteen pairs of uniaxial strain gages (at locations 01 to 15, base to top of pile) were installed lengthwise on the north and south surfaces of the steel pile to measure changes in strain along the length of the pile [Figure 2-6(b)]. An additional eleven accelerometers, unlabeled in Figure 2-5 and Figure 2-7, were installed at locations on the outside of the laminar soil box and the shake table surface. Six string potentiometers were attached to the reaction wall and measured the horizontal movement of the laminar frames. A seventh string potentiometer measured the horizontal displacement of the pile at approximately 89" from the bottom of the pile, and an eighth string potentiometer measured the horizontal displacement of the pile at the location of actuator loading.

Figure 2-4. Instrumentation of saturated soil layer and laminar soil box (elevation view)

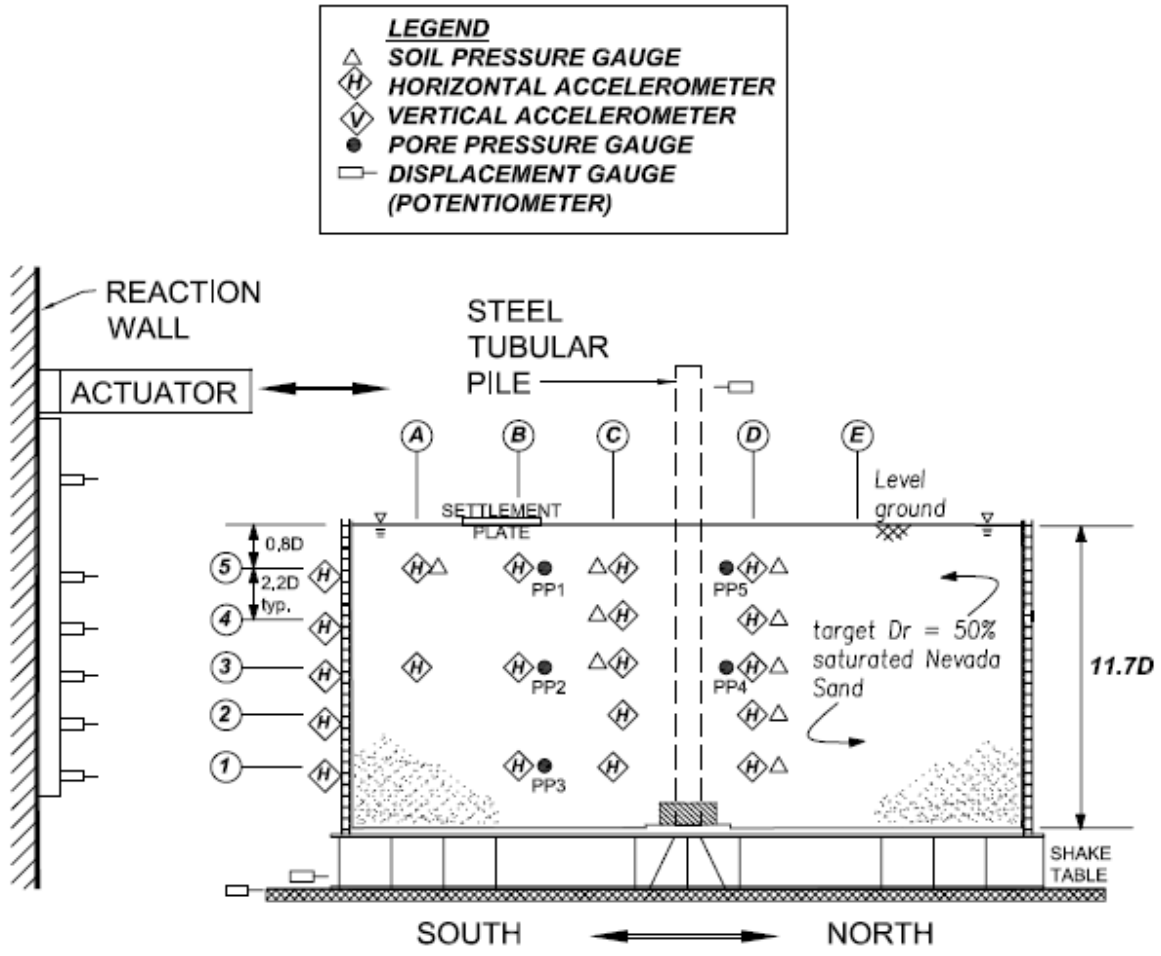

Figure 2-4: Lines 1 to 5 are vertically spaced at 13" O.C. Instruments at line A are 10D away from the pile face; instruments at line B are placed 6D from the pile face; instruments at lines C and D are placed 3D away from the pile face. Line E denotes the location of the CPT profiles and is located 6D from the pile face.

Figure 2-5. Instrumentation of saturated soil layer (plan view)

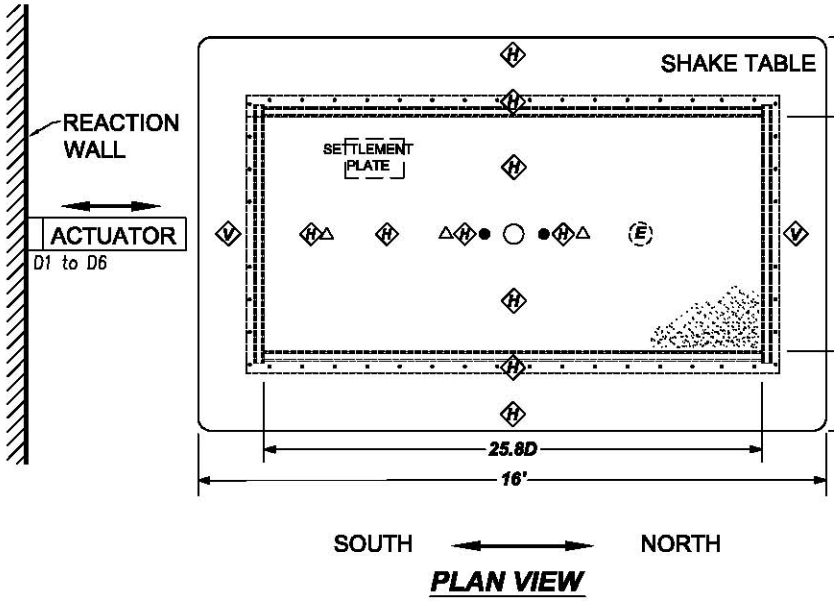

Figure 2-6. Instrumentation on steel pile

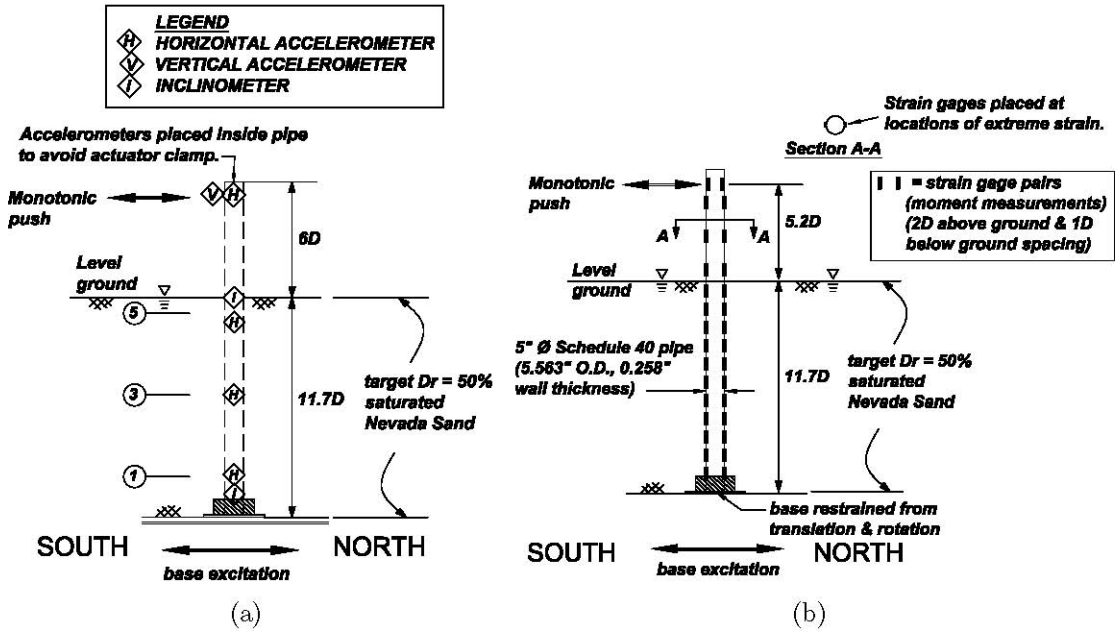

Figure 2-6: (a) accelerometers spaced vertically below the ground surface at 26" O.C. and (b) strain gages installed at north and south extreme sides of the steel pile.

Figure 2-7. Instrumentation of accelerometers in saturated soil layer

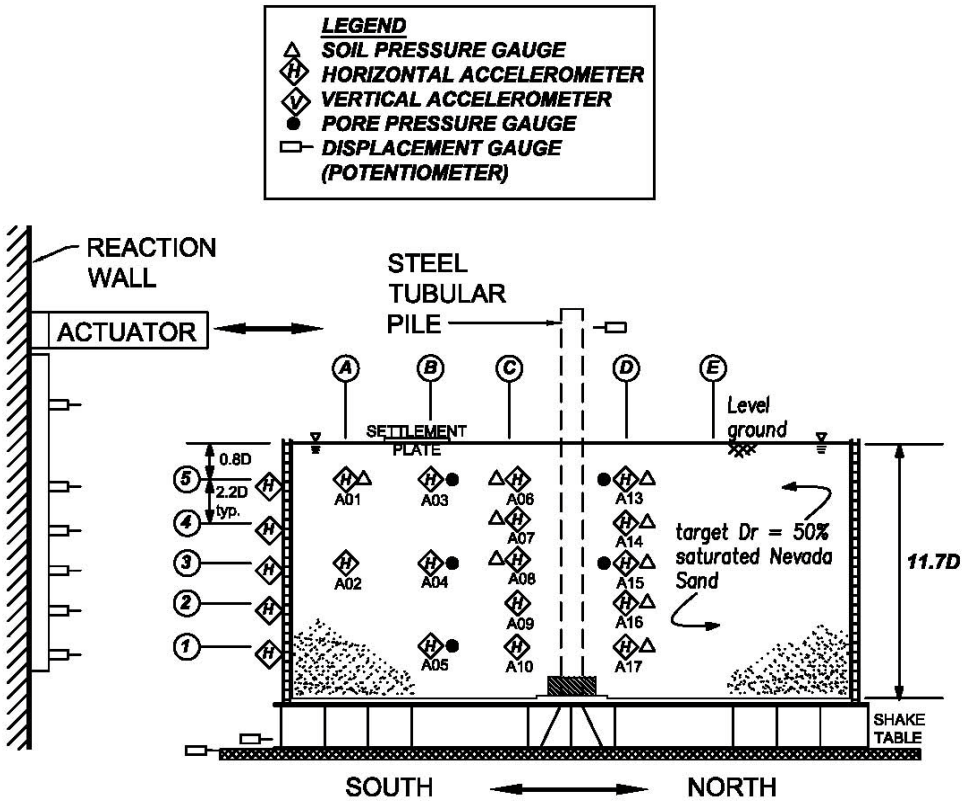

Figure 2-7: Accelerometers are placed within the saturated layer. Lines at 1 to 5 are vertically spaced at 13" O.C. Instruments at line A are 10D away from the pile face; instruments at line B are placed 6D from the pile face; instruments at lines C and D are placed 3D away from the pile face.

Figure 2-8. Accelerometers within the saturated soil layer (plan view)

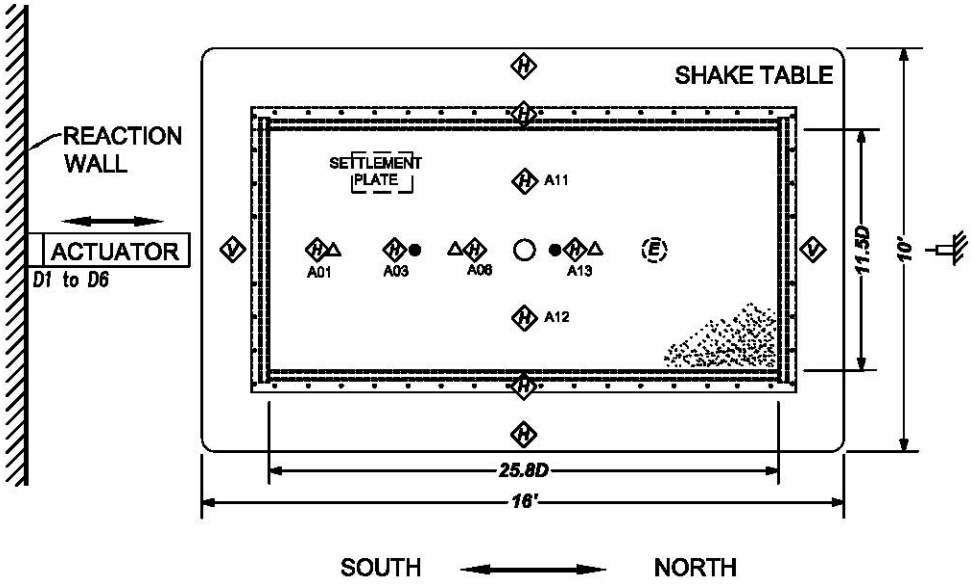

2.4 Model Design and Construction

The instrumented tubular steel pile was installed in the laminar soil box prior to placement of the soil. The base of the steel pile was fixed inside a steel collar, which, in turn, was bolted to the bottom of the laminar soil box, which was bolted to the shake table. The homogeneous saturated soil layer was placed using the aforementioned pluviation method (Section 2.2). While the soil layer was being placed, instrumentation was concurrently installed. The materials used and specific construction details are discussed in the following subsections.

2.4.1 Material Tests

The steel pile was a Schedule 40 ASTM A53 steel pipe with an outside diameter of 5.563" and nominal manufacturer's wall thickness of 0.258". Although the manufacturer indicates a nominal pipe thickness of 0.258", structural steel members are allowed a dimensional compliance of 92%. Measurements of at least 7 locations of actual pipe indicate a variation of 0.225" to 0.240". Milled test coupons, deemed to have a more accurate thickness than the pipe ends, which may have been filed after being sawn, had measured thicknesses of 0.240". This measured thickness of 0.240" conforms with dimensional tolerances.

Mill test certifications provided by the pipe supplier indicate that the material is grade B steel (heat #313712), with a yield strength of 52,937 and 55,112 psi for two samples tested. Ultimate tensile strengths are reported as 64,540 psi and 66,715 psi, at final elongation of 36% and 32%, respectively. Assuming that the yield stress from the mill certificate is at 0.002 strain, then the calculated Modulus of Elasticity ranges from 26,470 ksi to 27,560 ksi.

To characterize the material of the steel pile, three test coupons were milled from the same steel pipe from which the steel pile was constructed (Figure 2-9), and tension tests were performed on the coupons (Figure 2-10). The weld seam on the pipe was avoided in manufacturing the steel coupons. The gage length for each test coupon was 8" with a cross-sectional area of 0.36 square inches. Note that material coupons were not flat, and this is reflected in the zoomed in region on the left plot. The first portion of the curve at strains less than 0.0005 shows the region when the samples are straightened during the tension tests. At larger pre-yield strains, the curve is linear. This linear region is used to estimate the Modulus of Elasticity and to define the slope of the line used for the 0.2% offset method. Reported values of the strains in the following have subtracted out the contribution of strain associated with the flattening of the coupon (< 0.0005). Extrapolation of a straight line from the elastic portion results in an $E_{average} = 19500$ ksi. The 0.2% offset method results in an average yield strain and stress of 0.00486 and 60.2 ksi, respectively. The region where yielding occurs (the "corner") occurs over a strain range from 0.00255 to 0.00418 and an associated stress range of 49.1 to 60.1 ksi. The average ultimate stress is 67.6 ksi, and the average ultimate strain (as recorded by the extensometer) is 0.128 in/in. To avoid damage to the extensometer, it was removed just prior to fracture of the test coupons for each tension test (Figure 2-11).

In summary, the yield stress values from the mill certificate are comparable to that from the test coupons, however, the selection of yield strength and stress is dictated by the nonlinear local behavior at yield. Refined modeling may be achieved by utilizing the actual stress-strain material test data, which may be provided if needed.

Figure 2-9. Typical test coupon milled from steel pipe (Schedule 40 ASTM A53)

(a) Plan view of test coupon. (b) Cross-section of test coupon.

Figure 2-10. Stress-strain plots for steel coupons

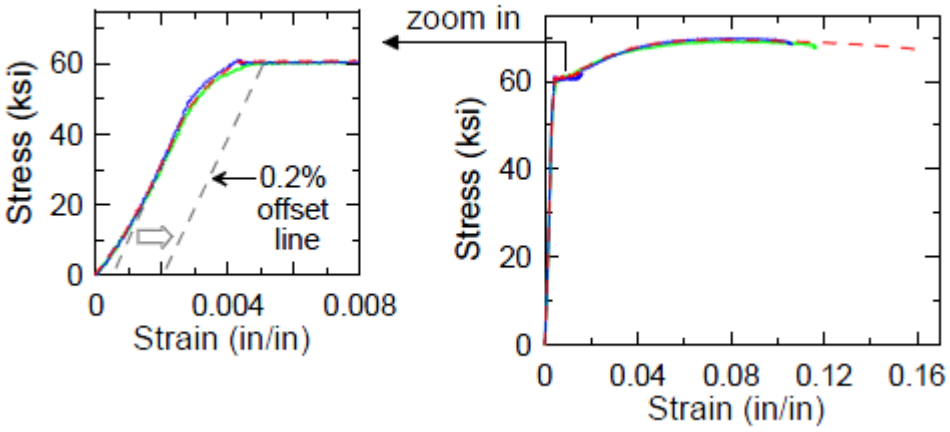

Figure 2-11. Tension tests on steel coupon

(a) Experimental setup for steel coupon.

(b) Typical fractured test coupon.

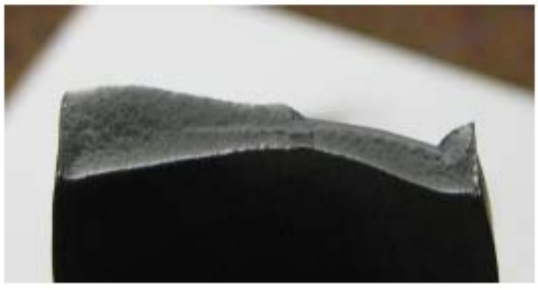

(c) Cross-section of typical fractured test coupon.

2.5 Pluviation Summary and Soil Characteristics

Nevada sand #60 was used for the saturated soil layer. This sand was supplied through a local distributor, Scott Sales Company, and was trucked to UCSD Powell Laboratories in large super sacks with an individual capacity of approximately 3000 lbs each. Sand in each sack was encased with an inner bag of plastic to prevent moisture from contaminating the kiln-dried sand. Subsequent deployment of the sand into the laminar soil box was through a cinch opening on the bottom of the sack. The local supplier obtained the Nevada sand from Simplot Silica Sand (Foundry Sand #60).

Samples of sand were provided to a local firm, Geocon, for basic index testing. This sand is visually observed to be poorly graded from the grain-size distribution curve (Figure 2-12), with D_{10} = 0.0045 inch, D_{30} = 0.0070 inch, D_{50} = 0.0088 inch, and D_{60} = 0.010 inch (ASTM D422-63). Note that the Simplot data is provided by the manufacturer (ASTM E11). The sand's coefficient of uniformity C_u is 2.2, which supports its poorly graded quality. The maximum and minimum dry densities were determined to be 110.03 pcf (ASTM D4253) and 97.27 pcf (ASTM D4254), respectively. The minimum and maximum void ratios were determined to be 0.494 and 0.690, respectively. The specific gravity of the sand was determined to be 2.64 (ASTM D854-06).

Placement of the Nevada sand in the laminar box was done in approximate five inch thick lifts using the previously described wet sedimentation method (Section 2.2). Lift thicknesses were approximated, as it was difficult to obtain a perfectly flat surface during pluviation; slight texture on the soil surface was unavoidable. Dry sand was dropped from the bag to the hopper, and sand was deployed from the tube to fall into the water in the laminar soil box (Figure 2-13). The average cumulative relative density of the box was approximately 41%, as calculated from the cumulative volume of dropped sand (43950 lbs) and estimated volume of the box (430.5 cubic feet) (Table 2-2). Note that slight uncertainties in volume measurements are anticipated due to linear undulations and unevenness of the top of the soil surface.

Figure 2-12. Nevada Sand #60 grain size distribution

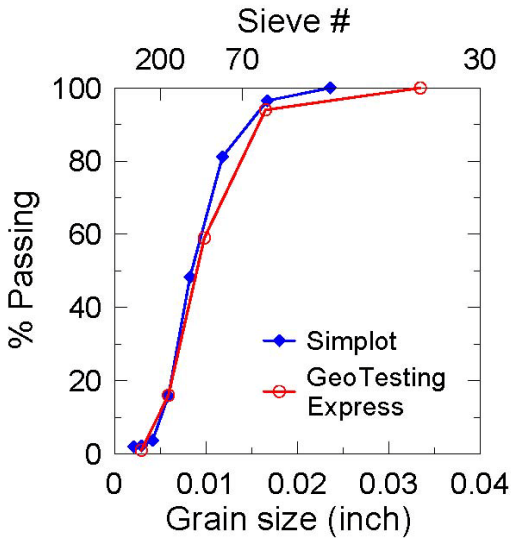

Table 2-2. Actual measured volumes and weights

Lift #	Cumulative Volume (ft^3)	Thickness (inch)	Cumulative weight (lbs)	Dry density (pcf)	Cumulative D_r (%)
1	31	5	3150	102.5	44
2	66	5.75	6775	102.5	44
3	101	5.75	10475	103.2	50
4	131	4.75	13200	101.0	32
5	161	5	16525	102.4	43
6	186	4	19000	102.1	41
7	217	5	21975	101.4	35
8	248	5	24950	100.8	30
9	272	5	27575	101.3	35
10	306	5.5	31800	103.9	55
11	337	5	34850	103.5	52
12	369	5.25	38350	103.9	55
13	400	5	40950	102.4	43
14	431	5	43950	102.1	41

Figure 2-13. Pluviation process for laminar soil box

Figure 2-13: (a) Setup; (b) Sand deployment from bag; (c) Sand falling into hopper; (d) Placement of sand in box; and (e) Lift of sand underneath standing water.

Upon completion of soil placement, cone penetration tests were conducted by Gregg Drilling using a mini cone assembly placed over the laminar soil box. These penetration tests were conducted on the centerline of the pile (in the loading direction), at a distance ranging from 2 to 3 feet away from the face of the pile and at times before and after testing of the specimen occurred (see Figure 2-4 and Figure 3-6). Average corrected tip resistance values for the North and South CPT1 locations were 9.06 tsf and 6.89 tsf, respectively (Figure 2-14). Average sleeve friction of the North and South CPT tests were 0.0089 tsf and 0.0074 tsf, respectively. The values for the sleeve friction were generally below 0.034 tsf (Figure 2-14). The maximum friction ratio was less than 1.0% with the average friction ratio at about 0.48% between the North and South locations.

For both CPT2 and CPT3, the cone penetration operator indicated he encountered a “hard object” at about 4 feet below the ground surface. Therefore, both records terminate at this elevation because the CPT operator wanted to avoid damage to the mini cone or any possible embedded instrument. Cone penetration test, CPT2, was conducted on the North side of the box (Figure 2-15) and at the end of the first day of testing. The average corrected tip resistance value for the CPT2 location was 12.9 tsf, while the average sleeve friction was 0.079 tsf. The maximum friction ratio was less than 1.0%, with the average friction ratio at about 0.40%. At the end of the second day of testing, cone penetration test, CPT3, was conducted on the North side of the box (Figure 2-16). The average corrected tip resistance value for the CPT3 location was 14.5 tsf, while the average sleeve friction was 0.036 tsf. The maximum friction ratio was generally less than 1.0%, with the average friction ratio at about 0.32%.

Figure 2-14. Results from mini-CPT tests performed by Gregg Drilling (CPT1)

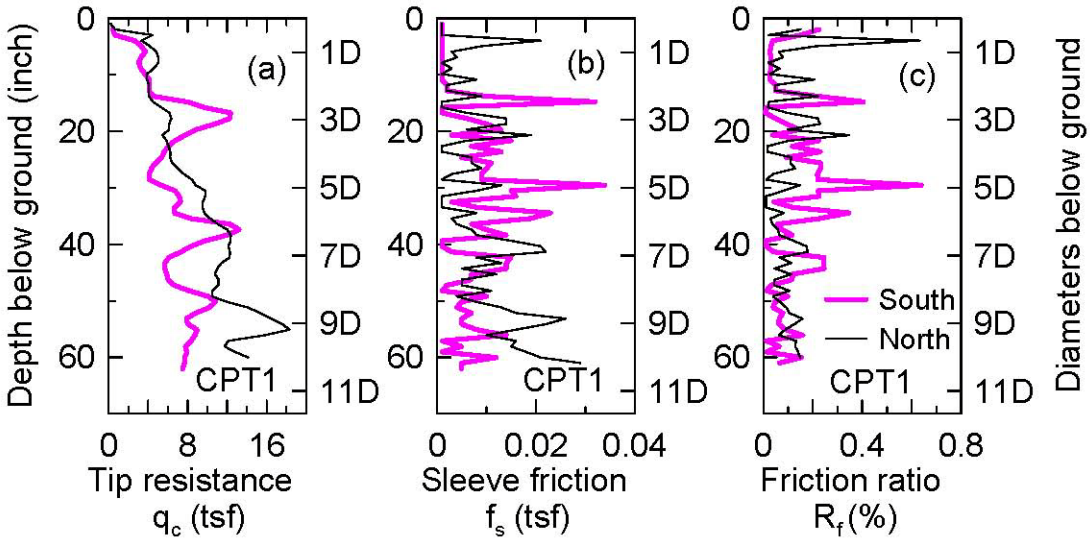

Figure 2-14: (CPT1, before testing of specimen): (a) corrected tip resistance, (b) sleeve friction, and (c) friction ratio.

Figure 2-15. Results from mini-CPT tests performed by Gregg Drilling (CPT2)

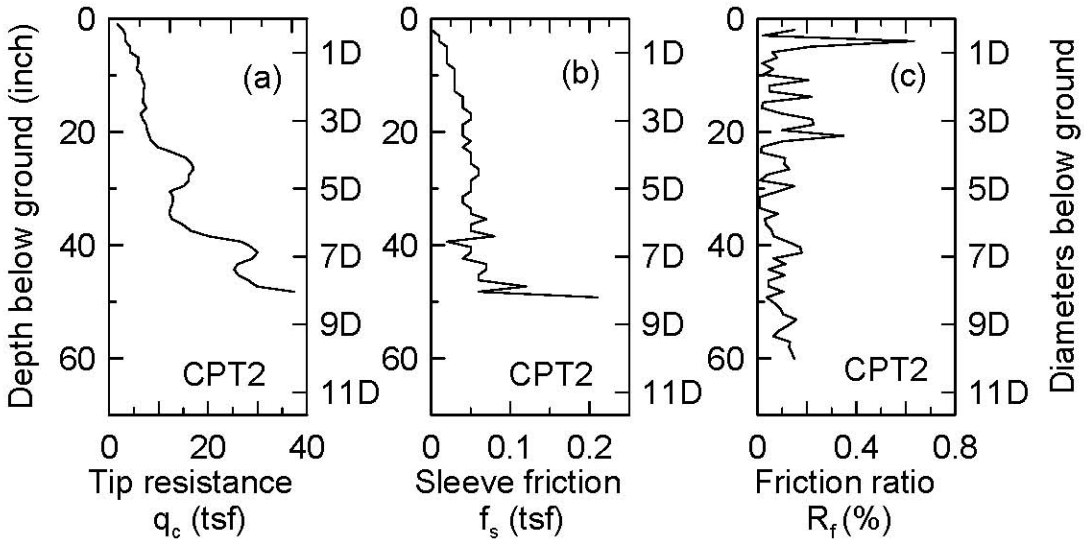

Figure 2-15: (CPT2, after first day of testing): (a) corrected tip resistance, (b) sleeve friction, and (c) friction ratio.

Figure 2-16. Results from mini-CPT tests performed by Gregg Drilling (CPT3)

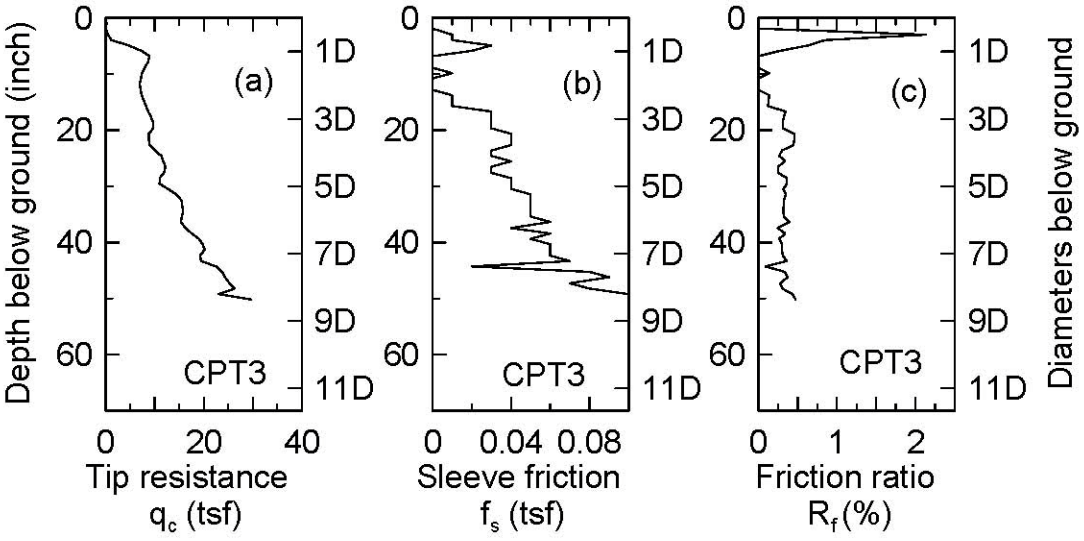

Figure 2-16: (CPT3, after second day of testing): (a) corrected tip resistance, (b) sleeve friction, and (c) friction ratio.

Using the correlations of Kulhawy and Mayne (1990) and Salgado and Prezzi (2007) with the corrected tip resistance, the relative density D_r on average (up the soil column) ranges between approximately 20-50% for CPT1 and between 30-60% for CPT2 and CPT3 (Figure 2-17 and Figure 2-18). It is noted that greater variability is observed on the South region of the box, which is attributed to this region being the access point for instrumentation and pluviation during construction. A relatively consistent distribution of D_r of 45% along the soil column is observed

on the North region of the soil box. These values are consistent with D_r values obtained using weight and volume measurements taken during soil placement, and slightly less than the target D_r. Recall that CPT2 was taken at the end of the first day of testing and that CPT3 was taken at the end of the second day of testing. Both CPT tests were taken only on the north side of the laminar soil box due to the actuator placement. Increasing relative density is generally observed.

The correlations for D_r are repeated here for completeness. The estimate from Kulhawy and Mayne (1990) is:

$$D_r(\%) = \sqrt{\frac{q_c}{305 Q_c}\sqrt{\frac{2000 lbs/ft^3}{\sigma'_z}}} \qquad (2.1)$$

where Q_c is a constant equal to 1.09, q_c is tip resistance is in units of tsf, and σ'_z is vertical effective stress in units of psf. The correlation for the relative density is from the result of 24 sets of calibration chamber tests on fine to medium sands, mostly clean quartz specimens. Most sands were placed by dry-state air pluviation and most of the CPT tests were performed on dry sands.

Figure 2-17. Comparison of average relative density, North boring, and South boring for CPT1

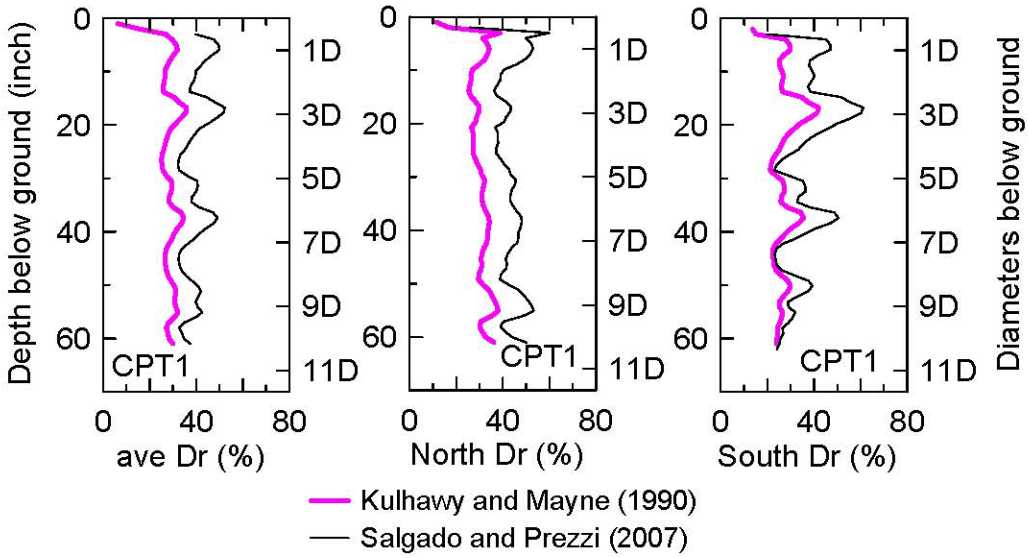

Figure 2-18. Comparison of relative density, North boring only for CPT2 and CPT3

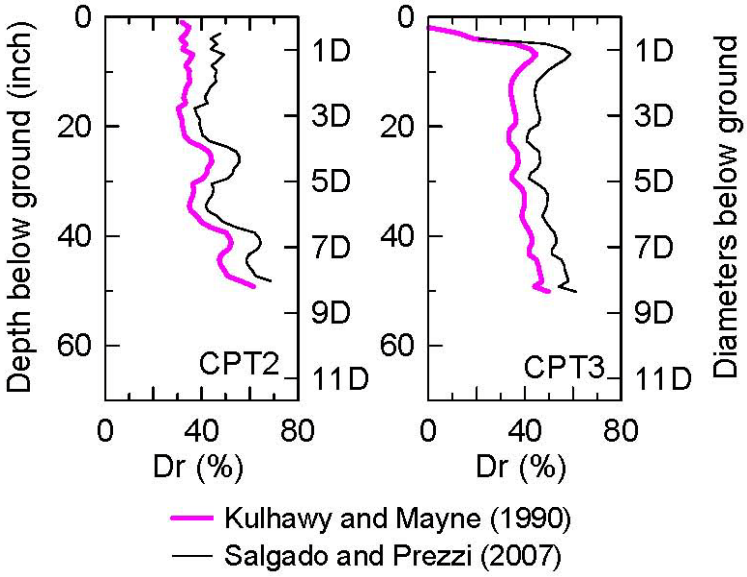

Salgado and Prezzi (2007) is as follows:

$$D_r(\%) = \frac{\ln \frac{q_c}{p_a} - 0.4947 - 0.1041\phi_c - 0.841 \ln \frac{\sigma'_h}{p_a}}{0.0264 - 0.0002\phi_c - 0.0047 \ln \frac{\sigma'_h}{p_a}} \qquad (2.2)$$

where p_a is atmospheric pressure of 1 tsf, q_c is tip resistance in tsf, σ'_h is horizontal effective stress in units of tsf, and $\neq_c$ is the critical state friction angle of the sand. Equation 2.2 is developed from reconstituted silica sand samples in calibration chamber tests [Lee et al. (1999); Salgado et al. (1997)] with some saturated samples.

Due to the natural testing sequence, the soil was densified as testing progressed. The most significant densification is observed following dynamic A (comparison of CPT 1 and 2, Figure 2-19). One may be interested in characterizing the soil layer into its upper and lower half (Figure 2-19 and Table 2-3). With this division, CPT1 indicates an average relative density of the North boring of 42% for the upper half and 45% for the lower half of the profile, while the South boring has an average relative density of 39% in the upper half and 32% in the lower half. For CPT2, the relative density for the above mid-height section of the box is 45% and below mid-height is 61%. For CPT3, relative density for the above mid-height section is 47% and the below mid-height relative density is 54%. For both CPT2 and CPT3, these averages do not include the bottom-most portion of the soil layer that was not measured by the mini cone penetration test. One may conjecture that this unmeasured bottom-most portion of the saturated soil layer had a relative density equal to or greater than the measured upper portions.

Figure 2-19. Comparison of relative density for CPT1 (North and South), CPT2 (North), and CPT3 (North)

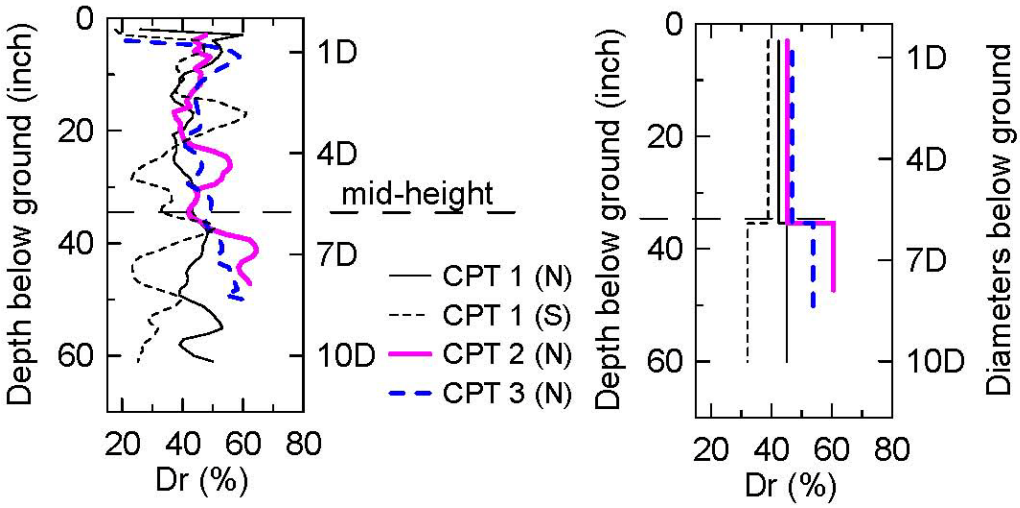

Figure 2-19: [Correlation of CPT data to relation of Salgado and Prezzi (2007)]

Table 2-3. Summary of mid-height relative densities for CPT1, CPT2, and CPT3

Depth Range	CPT1 North D_r(%)	CPT1 South D_r(%)	CPT2 D_r(%)	CPT3 D_r(%)
Upper half	42	39	45	47
Lower half	45	32	61	54

2.5.1 Shear Wave Velocity

Shear wave velocity for the saturated soil layer was estimated by hammer tests and also by correlations with soil characteristics. These methods give a range of average shear wave velocity from 250 ft/s to 475 ft/s. A summary of the methods used and resulting average shear wave velocity υ_s is provided in Table 2-4.

Table 2-4. Shear wave velocity estimates

Method	υ_s(ft/sec)
Seed and Idriss (1970)	
CPT 1	335
CPT 2	347
CPT 3	350
Bartake and Singh (2007)	250
Hammer tests	475

Hammer tests for measuring the shear wave velocity were able to obtain an average shear wave velocity of 475 ft/s. These hammer tests were implemented by placing a heavy steel plate on the surface of the saturated soil layer and striking the edge of the plate in a direction parallel to the ground surface and recording the arrival time of the waves generated at accelerometers (sensors A03 and A04) placed on the South side of the laminar soil box. Signal attenuation prevented the use of accelerometer A05. Results obtained may be of limited reliability due to the small size of the box. A

smaller sized box may cause excessive amounts of interference and complicate the determination of individual wave arrivals. The measured shear wave velocity from hammer tests ranged from 320 ft/s to 639 ft/s, resulting in an average shear wave velocity of 475 ft/s. Excluded from this data are aberrant values.

Estimates of the maximum shear modulus and the shear wave velocity were calculated with semi-empirical methods. These methods depend on calculating the maximum shear modulus G_{max} from available data and then estimating the shear wave velocity υ_s as the equation:

$$v_s = \sqrt{\frac{G_{max}}{\rho}} \tag{2.3}$$

For example, one may estimate the maximum shear modulus G_{max} as (Seed and Idriss, 1970):

$$G_{max} = 1000 K_{2,max} \sqrt{\sigma'_m} \tag{2.4}$$

From the dropped weight of the sand and the measured settlement during testing, an average void ratio and an average relative density of the saturated soil layer was estimated. From this data, a $K_{2,max}$ was estimated: for CPT1, $K_{2,max}$ = 45.4; for CPT2, $K_{2,max}$ = 48.9; and for CPT3, $K_{2,max}$= 49.6. Mean effective stress σ'_m was also calculated accounting for the densification of the sand, using measured settlement values. This method results in an average of G_{max}= 224 tsf and υ_s = 335 ft/s for CPT1, averages of G_{max} = 243 tsf and υ_s= 347 ft/s for CPT2, and G_{max} = 247 tsf and υ_s = 350 ft/s for CPT3.

The method of Bartake and Singh (2007) was also considered to estimate the shear wave velocity of the sand. Bartake and Singh (2007) use cylindrically molded sand specimens (dry and saturated) with bender elements to measure shear wave velocity at varying void ratios for three grades of quartz sands. The following expression is suggested:

$$v_s = A(D_{50})^{-B} \tag{2.5}$$

where A = 85-40*e* (where *e* = void ratio) and B = 0.15 for saturated sands. Equation 2.5 yields a shear wave velocity of approximately 250 fps for the saturated soil layer. An initial and final void ratio range of 0.610 and 0.588 was observed during testing, and a D_{50} of approximately 0.0088" was obtained from the gradation curve for the Nevada Sand #60.

2.5.2 Degree of Saturation of Soil Layer

Following sand placement, tests were conducted to measure the P-wave velocity in an effort to provide an indication of the degree of saturation of the soil layer. The south side of the box was impacted at specific locations with a 3 lb hammer and the wave's response in the soil was monitored with the soil-embedded accelerometers, recording at 3125 scans per second. Locations

(1 through 5) as indicated in the photograph in Figure 2-20(a) were struck with the 3 lb hammer in 3 sets of 5 blows at each location.

Accelerometers on the south side of the box were recorded [Figure 2-20(b)]. Using measured accelerations and tracing the wave propagation, P-wave velocities are estimated to range from 3000 ft/s to 6040 ft/s. The average of the obtained P-wave velocities is 5040 ft/s. Theoretically, this is higher than expected if the P-wave velocity is calculated from the average shear wave velocity and Poisson's ratio υ with the correlation:

$$\frac{v_p}{v_s} = \sqrt{\frac{2-2\nu}{1-2\nu}} \tag{2.6}$$

This ratio $\frac{v_p}{v_s}$ is 1.87 using υ = 0.3. With this correlation, a shear wave velocity in the range of 250 ft/s to 475 ft/s either appears to be too low, or an average P-wave velocity of 5040 ft/s appears too large. However, this correlation is not for saturated sands and is based on the assumption that the material is an isotropic, linear, elastic solid. An investigation by Matthews (1982) presents experimental data of shear wave velocity and P-wave velocity in soft saturated sediments (silts and sands). This experimental data gives a ratio of $\frac{v_p}{v_s}$ equal to or greater than 18, which shows the effect of saturation on the wave velocities. Thus, an average P-wave velocity of 5040 ft/s from the hammer test is reasonable.

There may be some uncertainty and associated error in the P-wave calculation, including estimating the exact start of the wave, which becomes more difficult as the pulse diminishes greatly over short distances. In Figure 2-21, the acceleration pulses from three accelerometers are shown as an example. These three accelerometers are at approximately the same vertical elevation and were used to determine the horizontal propagation of the P-wave velocity. Accelerometer A02 is closest to the hammer strike zone on the outside of the laminar soil box; accelerometer A04 is between A02 and A08; and accelerometer A08 is the farthest from the hammer strike itself. Note that the magnitude of the beginning of the pulse for A08 is the smallest of the three. Also, the pulses for A04 and A08 are more jagged and noisy than A02; this suggests that some information is being lost due to either the rate of data capture, interference from reflected waves, and/or diminishing intensity of the wave. At 3125 scans recorded per second, a data point is collected every 0.00032 seconds. While this may seem very fast, if the P-wave is traveling at 5000 ft/s, then it takes 0.001 seconds to travel across a distance of 5 feet. Since A02 and A08 are separated by less than 5 feet, then there is only a lag of approximately 2 or 3 data points that may occur between initial pulses. Recorded data points also do not correspond exactly to the start of the pulse because of diminishing intensity being overpowered by noise in the signal. These factors are what constrain the accuracy of the P-wave velocity measurements despite optimization of the instrumentation and data capture. Regardless, it is generally felt that a high degree of saturation was present in the saturated soil layer.

From the correlations between P-wave velocity and the pore pressure coefficient B and between B and the degree of saturation, for this soil, the range of P-wave velocity indicates pore pressure coefficients ranging from 0.986 to 0.997. These pore pressure coefficients indicate close to 100% saturation [Yang and Sato (2000); Yang (2002)]. As the degree of saturation of the soil layer decreases, its resistance to liquefaction increases; therefore, this test seeks a high degree of saturation approaching 100%.

Figure 2-20. P-wave experimental setup

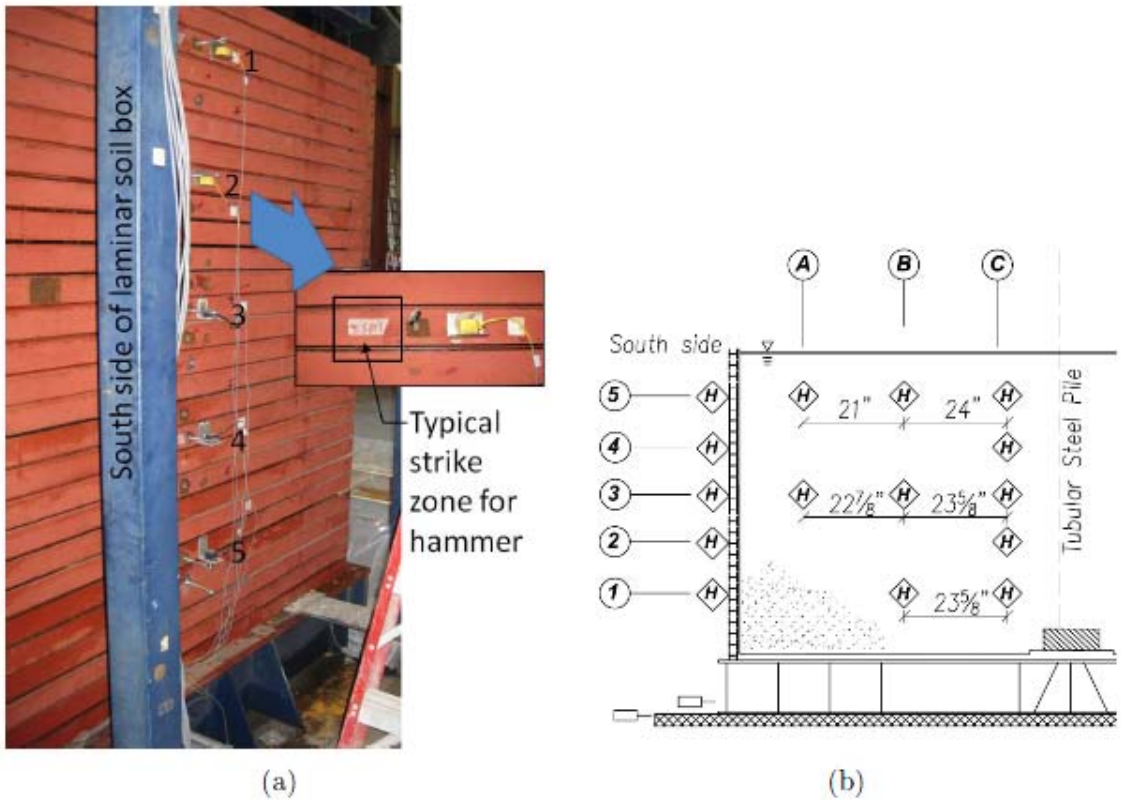

Figure 2-20: (a)South side of box with hammer strike zones indicated and (b) schematic of south side of soil box.

Figure 2-21. Sample acceleration pulses from accelerometers used for determining p-wave velocity

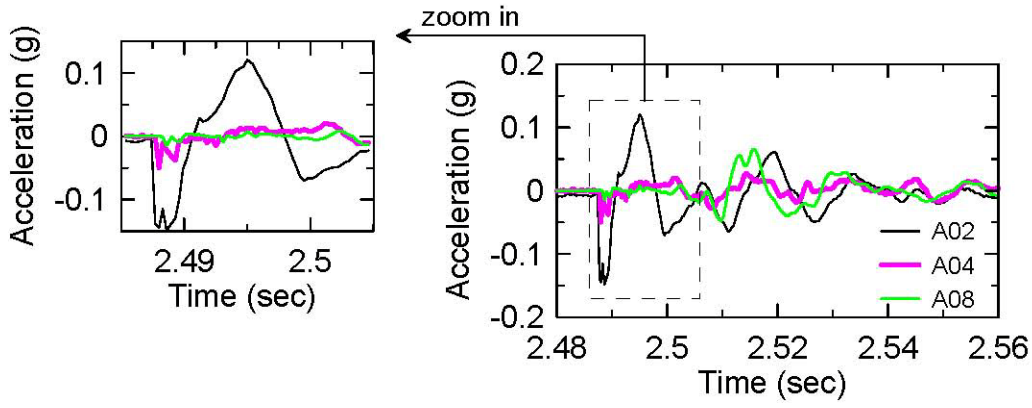

2.5.3 Dynamic Characteristics of the Pile-Soil System

Non-destructive (modal) hammer tests on the pile-soil system were conducted to obtain the natural frequency of the system prior to testing. The steel pile was struck with an instrumented hammer, and the results indicate that the system has a natural frequency of 32.8 Hz and damping ratio of 5.2% (Figure 2-22).

Figure 2-22. Non-destructive hammer test on pile soil system to obtain the natural frequency

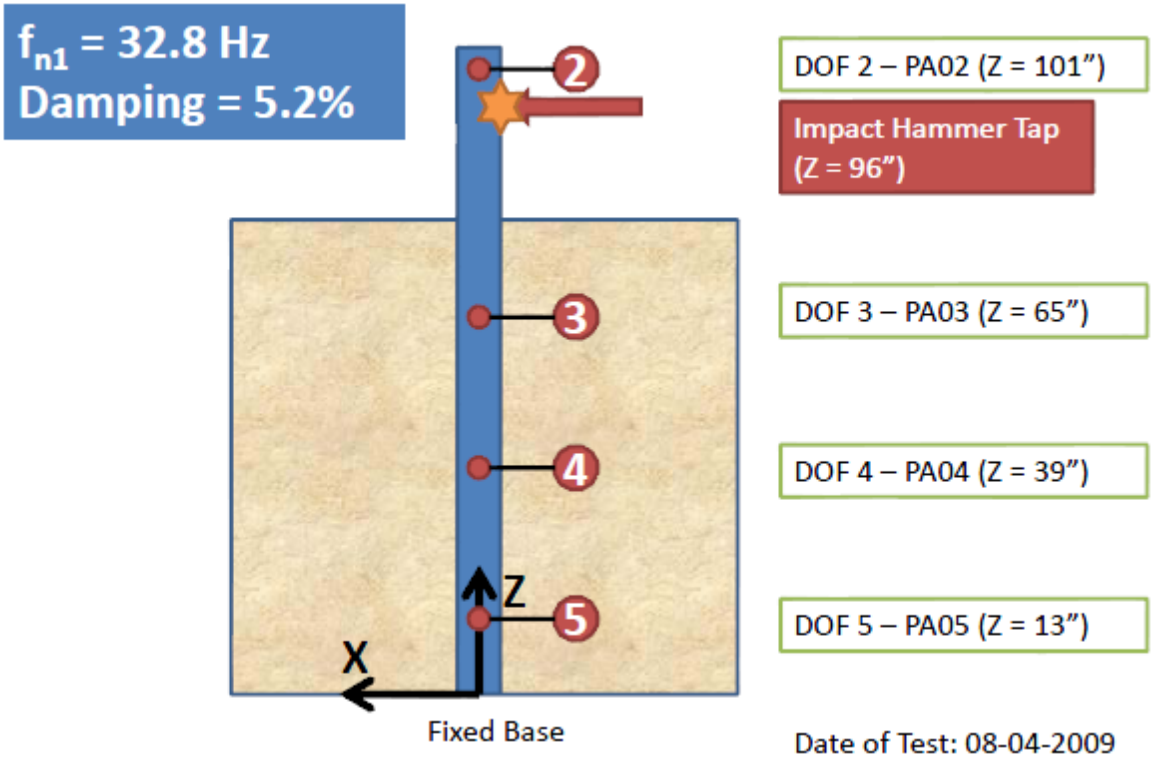

3. Test Procedure and Results

3.1 Test Protocol

The objective of this project is to experimentally determine nonlinear p-y curves at various levels of earthquake-induced excess pore pressure. Therefore, the test program was conducted in several distinct phases. Importantly, dynamic base shaking was first applied, with subsequent lateral loading of the pile head. Dynamic base shaking was applied to generate a minimum of three target excess pore pressure ratios (desired targets of r_u = 25%, 50%, and 90%). Upon reaching these target ratios, the pile was attached to a hydraulic actuator at its head and laterally loaded monotonically to induce inertial-equivalent response.

Testing of the specimen occurred over a two day period (Table 3-1). Day 1 was comprised of ground motion dynamic A and static push A. Following Day 1, a thin, low permeability cement-sand slurry layer was placed over the model to minimize pore pressure dissipation upward in the model. Day 2 was comprised of dynamic B and static pull B, followed by dynamic C and static push and pull C. Load protocols for these tests are detailed in Table 3-2 and Table 3-3. The static loading rate was 0.01 inches/seconds, and recorded data was collected at a rate of 5 points per second. During dynamic testing, data was collected at a rate of approximately 200 points per second.

It is noted that due to the stick-slip nature of the UCSD bearing-based shake table, the target dynamic shakes were difficult to achieve. This problem is complicated by the fact that the shake table could not be moved and hence the support bearings were not lubricated to provide fidelity prior to testing, as this would disturb the low confining stress model. Dynamic A with a target 9 cycles at 1Hz and 0.05g amplitude was predicted using the updated procedures of Idriss and Boulanger (2008) to achieve an average r_u = 25% within the soil layer. Dynamic A resulted in significant overshoot of the target (larger than anticipated amplitude and greater than target cycle count) and hence fully liquefied the model approximately 7 seconds into the record. The overshoot observed in test dynamic A was compensated for in dynamic B by reducing the predicted number of cycles by 1/3 and reducing the amplitude by 1/4. Upon completion of dynamic B, the target number of cycles was slightly increased for dynamic C to attain higher r_u values. It is noted that between 4 to 5 very small (less than 0.02g) trailing cycles are observed in dynamic B and C as the table attempted to re-center itself following the input shake.

Table 3-1. Chronology of test protocol

Day #	Protocol Name
Day 1	Dynamic A
	Static A
Day 2	Dynamic B
	Static B
	Dynamic C
	Static C

Table 3-2. Static testing protocol

	Static A	Static B	Static C
Maximum pile head displacement	1.0 inch	2.0 inches	4.5 inches

Table 3-3. Dynamic testing protocol (input)

	Dynamic A	Dynamic B	Dynamic C
Amplitude	0.05g	0.013g	0.013g
Ramp up and down cycles	3	0.5	0.5
Constant amplitude cycles	3	1	2
Total cycles	9	2	3
Duration	9 sec	2 sec	3 sec

Figure 3-1. Dynamic A input motion time history (input shown in pink)

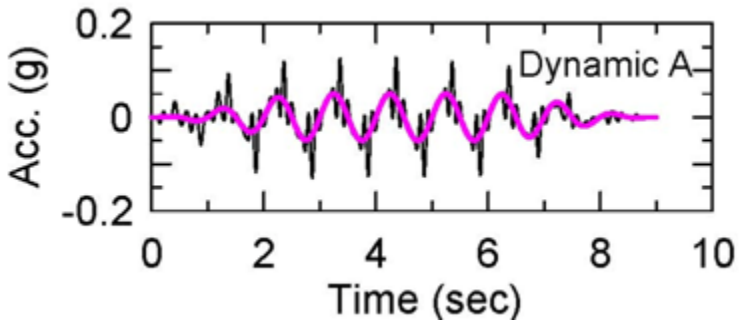

Figure 3-2. Dynamic B input motion time history (input shown in pink)

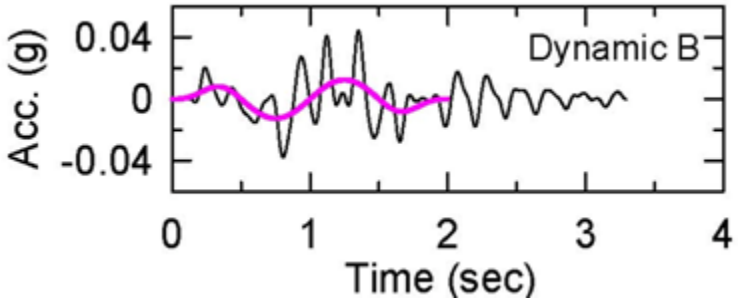

Figure 3-3. Dynamic C input motion time history (input shown in pink)

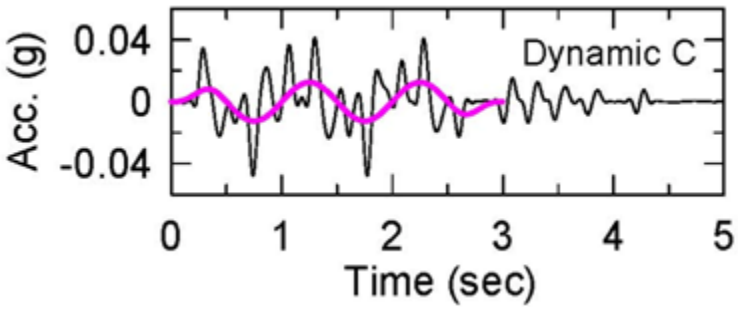

During testing, the settlement of the soil layer was measured by a settlement plate. From the measured settlement, an average relative density is estimated from the weight of the dropped sand and the change in volume of the saturated soil layer in Table 3-4.

Table 3-4. Settlement of saturated soil layer and average D_r (%) from dropped weight of sand

Test	Settlement (inch)	Average D_r (%)
Before testing	0.0	41
Dynamic A	0.766	50
Dynamic B	0.017	50
Dynamic C	0.170	52

3.2 Experimental Results

3.2.1 Push Test on Pile Absent Soil

Before placement of the saturated soil layer, a push test was conducted on the pile to characterize the rotational stiffness of the pile as anchored in its collar at the base of the laminar box. The pile was fixed at the base in a steel collar and secured by concrete [Figure 3-4(a)]. For the push test, the actuator was attached to the top of the pile [Figure 3-4(b)]. The data in Figure 3-5, in the clockwise direction, indicates the progression of the push test, namely, the pile was (1) pushed by the actuator, (2) pulled back to its initial position, (3) pulled by the actuator, and then (4) pushed back to its initial position. Horizontal and vertical displacements at certain locations on the pile were recorded during the push test. The input load level was well below the yield strength of the pile. The push test was displacement controlled and taken to approximately $0.3\ \Delta_y$, where Δ_y is the theoretical yield displacement of the pile in a cantilever position.

Results from the push test indicate symmetric behavior for the steel pile in collar system. Minor pinching of the hysteresis is observed in the plot of shear force versus displacement at the top of the pile, although no damage was readily observed at the pile to collar connection. Despite the absence of apparent visual damage, inspection of the vertical and horizontal displacement data reveals that a gap formed at the pile to collar connection. Back-calculation from the displacement data indicates that an equivalent gap of approximately 1/16" formed at the pile to collar connection from a combination of vertical uplift and horizontal movement of the pile when the pile was pulled or pushed back toward its initial position. The gapping was not observed when pushed or pulled from its initial position; it only manifested after the peak displacement or load was reached, and the pile was returned to zero displacement. This indicates that the pile was re-seating itself in the collar.

Further investigation reveals that rotation occurred between the collar and the base plate of the laminar soil box. This phenomena is believed to not be attributed to pile flexure or collar-to-pile gapping, but rather this unexpected amount of pile rotation was due to the collar-to-box connection. This rotation at the base of the pile affects the actuator measured and strain gage calculated response of the pile-soil system and is discussed later in this report. See section 3.2.6 for more details.

Peak force and displacement in the positive (push) direction were 0.471 kips (0.3 V_y)and 0.96" (0.3 Δ_y). Peak force and displacement in the negative pull direction were -0.452 kips (0.3 V_y) and -0.90" (0.3 Δ_y). This results in a secant stiffness of approximately 0.5 kip/inch, which includes the gap. Excluding the gap, the stiffness on the 1st push is 0.49 kip/inch; the stiffness on the 2nd portion (pull back toward initial position) is 0.66 kip/inch; the stiffness on the 3rd portion (pull from initial position) is 0.44 kip/inch; and the stiffness on the 4th portion (push back toward initial position) is 0.63 kip/inch.

Based on data from the material tests, the theoretical stiffness for the cantilever steel pile is 0.50 kip/in, using an estimated length of 96.5 inches. Using the experimental stiffness from the peak force-displacement plots to back calculate the effective length of the pile, one obtains an effective length ranging from 88 to 100 inches, the average of which is 94 inches. With the slight gap that occurs at the pile to collar connection and the rotation at the base, the pile system is not a true cantilever system. When the pile is pushed or pulled from its initial position, the pile system is slightly softer than expected. When the pile is returned to the initial position, the pile system is slightly stiffer, and then the gap is closed. Similar gapping may be expected when the pile is surrounded by soil, thus it should be accounted for in modeling the soil-pile system.

Figure 3-4. Push test experimental setup

(a) Base of pile to collar connection.

(b) Actuator attachment to pile top.

Figure 3-5. Actuator load versus top of pile displacement -push test without soil

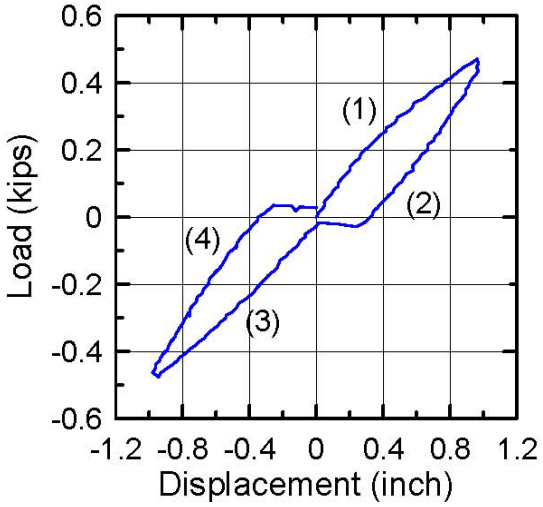

3.2.2 Dynamic Events: Pore Pressure Time Histories

Pore pressures in this section are evaluated in two distinct approaches. First, they are presented for the history of construction and testing of the model. Second, pore pressures for each of the dynamic-static testing phases (namely A, B, and C) are individually presented. The former, termed "test program duration pore pressures" is important as it assists with characterizing the change in pore pressure due to potential movement of the sensors, as well as intermittent construction, and/or power fluctuations. The latter, denoted as "series A (or B, C) duration pore pressures", is needed to determine the build-up and eventually the actual pore pressures at the start of lateral loading of the pile. It is important to note that during testing two different data acquisition systems were needed, one for dynamic recording, another for static recording rates. Moreover, attachment of the pile to the hydraulic actuator was facilitated following the dynamic tests.

The test program duration pore pressures for each of the sensors are provided in Figure 3-6 to Figure 3-10. These measurements document the pore pressures from the moment the water elevation is at that of the particular sensor, through construction and testing of the specimen. The consistent draw down at 800 hours into the construction is attributed to a power loss and is noted to have not affected measurements, as all sensors retained their prior values. This is indicated by the dashed gray line.

Following shaking on day 1 and prior to placement of the impermeable layer, at approximately 1050 hours, the consistent reduction in pore pressures is attributed to removal of excess water to prepare and re-level the specimen prior to the impermeable layer pour. Then at approximately 1075 hours, it is noted that approximately 15 hours after the impermeable layer was placed (at approximately 1060 hours), cement hydration likely drew water from the upper layers, therefore temporarily reducing the pore pressure.

Figure 3-6. Test program duration pore pressure time history for instrument PP1

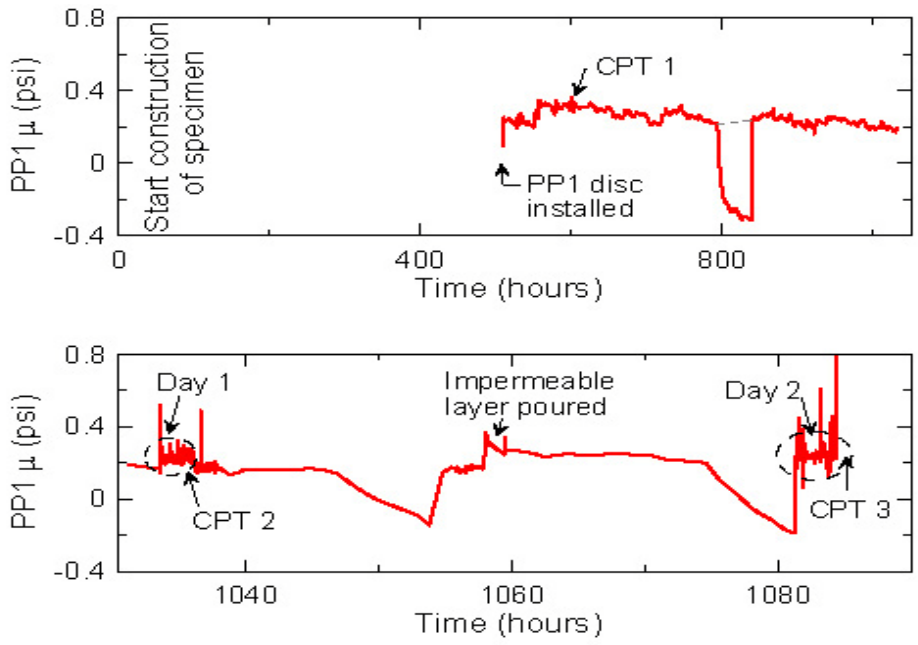

Between day 1 and day 2 of testing, a thin impermeable layer was poured onto the top of the saturated layer. Details of the mix are presented in Table 3-5. The water cement ratio was 0.71; the mixture was very liquid. The slump test gave a value 10.5" and formed a roughly circular puddle with an average diameter of 22.5". Material tests for the impermeable layer on day 2 indicate a compressive strength of 1.66 ksi in the morning and a compressive strength of 2.01 ksi in the afternoon (at the end of day 2 testing).

Event A-C duration pore pressures are shown in Figure 3-12 - Figure 3-14. These plots show sensors initially placed at a common elevation in pairs, (i.e. sensors PP1 and PP5; and PP2 and PP4 are placed on the same plot). An excess pore pressure ratio r_u is estimated by tracing the pore pressure history and accounting for the final observed position of the sensors, as shown on the right of each figure, for each sensor. The excess pore water pressure ratio r_u is calculated by

Figure 3-7. Test program duration pore pressure time history for instrument PP5

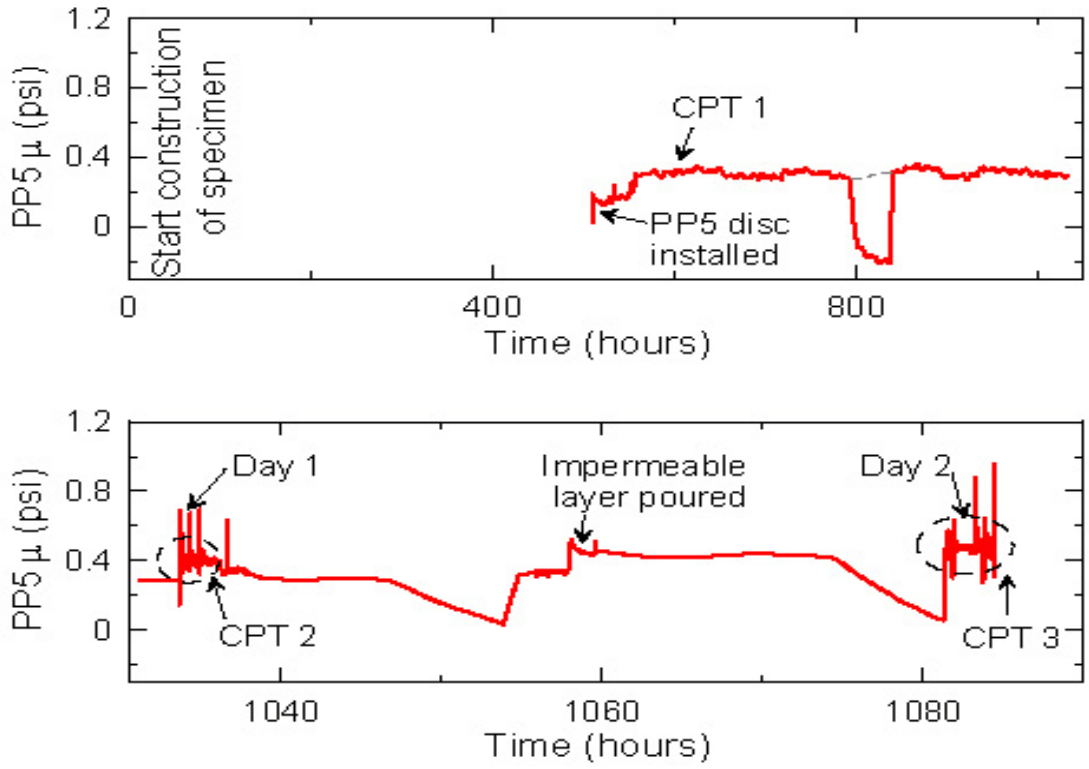

Figure 3-8. Test program duration pore pressure time history for instrument PP2

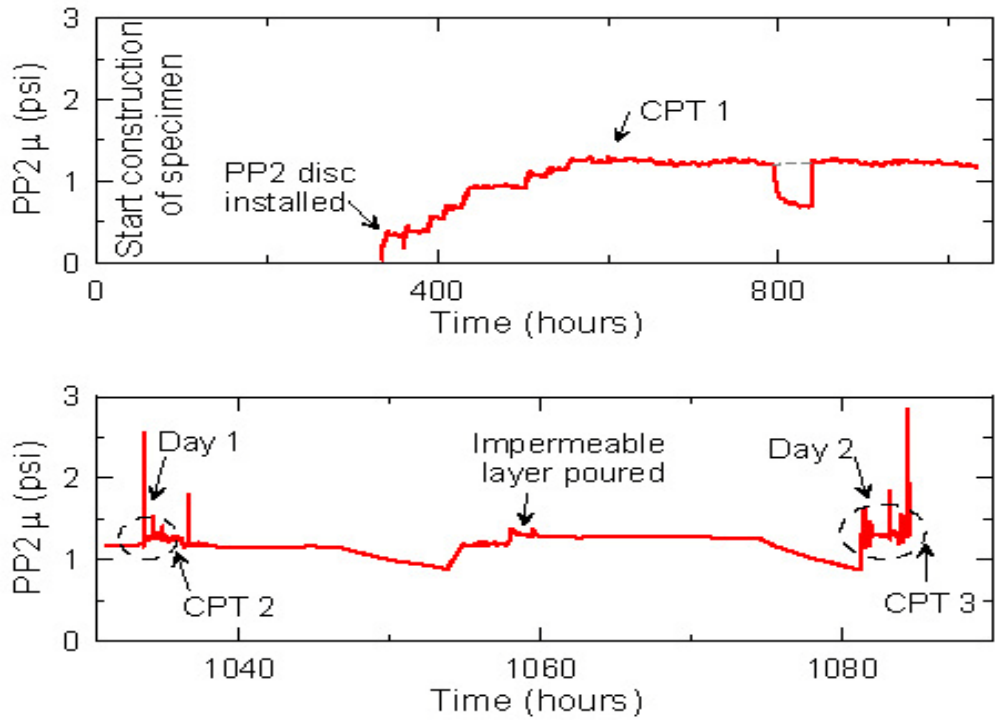

Figure 3-9. Test program duration pore pressure time history for instrument PP4

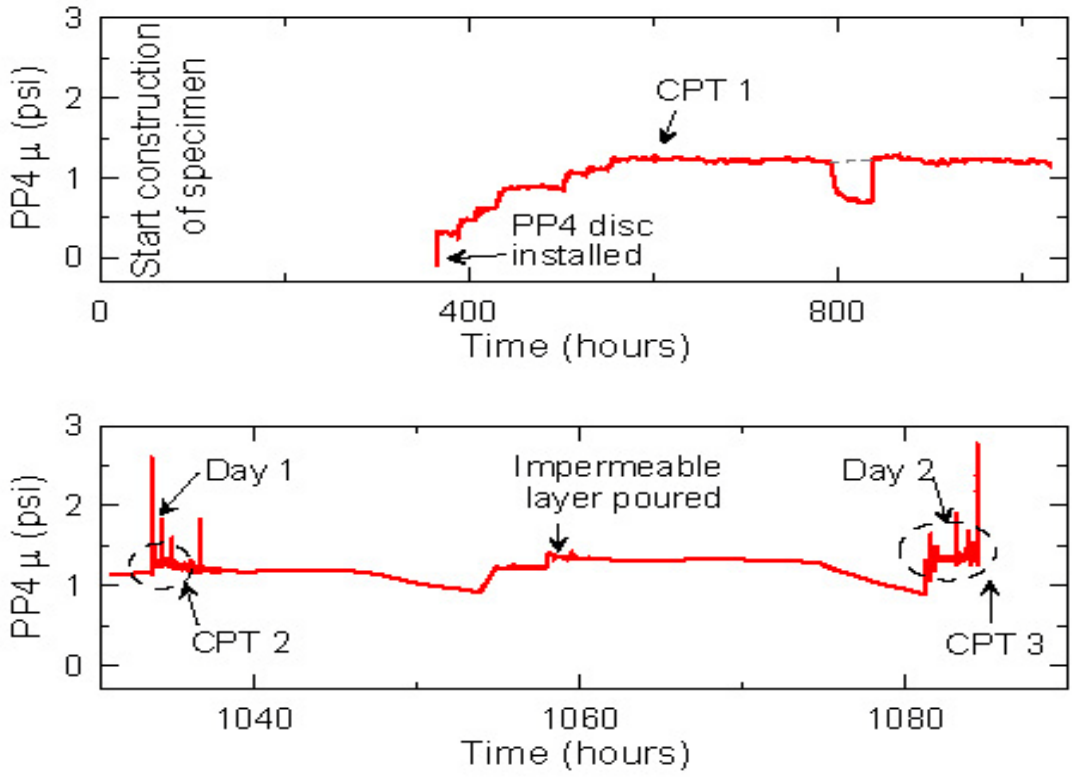

Figure 3-10. Test program duration pore pressure time history for instrument PP3

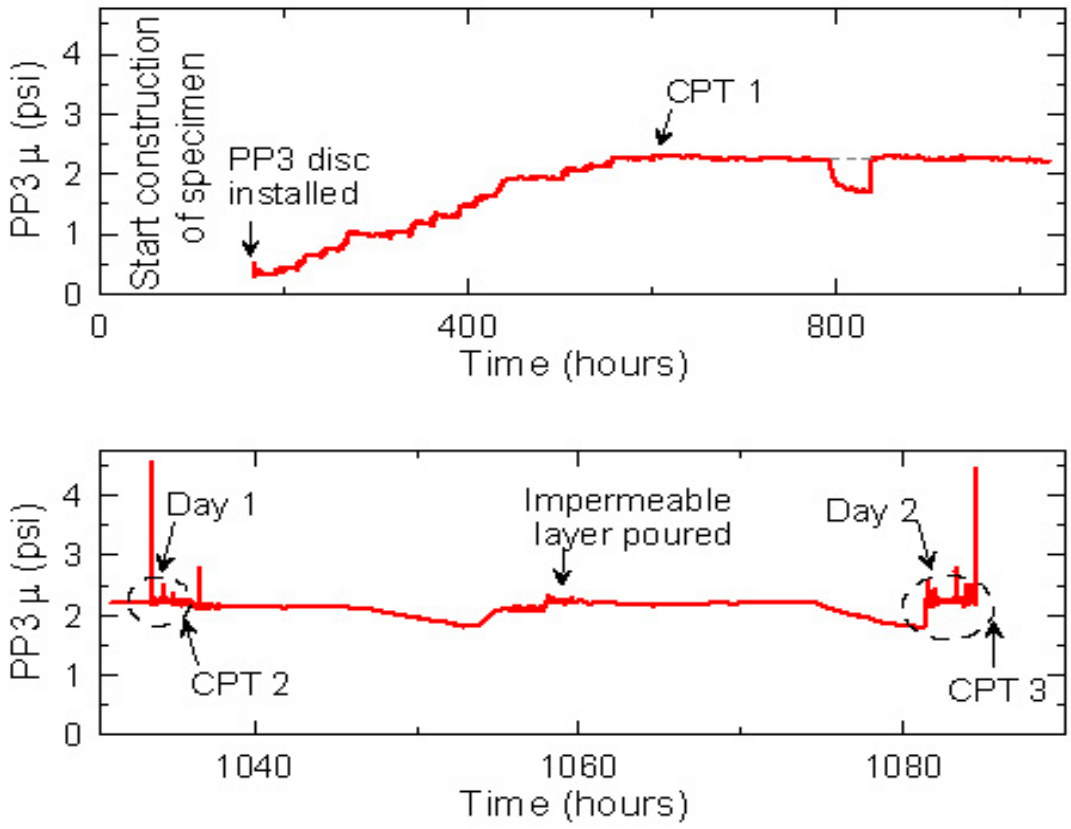

Table 3-5. Design mix for thin crust

Material	Weight per cubic yard
Cement	609 lbs
Fly ash	143 lbs
3/8" x #8 aggregate	1423 lbs
Fine aggregate	1348 lbs
Water	433 lbs
WRDA 64 (admixture)	19.0 oz
ADVA-HRWR (admixture)	45.0 oz

taking the difference between the initial and current pore pressure and dividing by the vertical effective stress, i.e.

$$r_u(\%) = \frac{(\mu - \mu_o)}{\sigma'_v} \tag{3.1}$$

where μ_o = initial pore water pressure, μ = current pore water pressure, and σ'_v = vertical effective stress.

Excavation of the specimen after testing revealed that pore pressure instrumentation had shifted slightly from initial positions. Initial positions of the pore pressure instruments were back-calculated from the initial pore pressure values. The initial and final vertical depths below ground surface are tabulated in Table 3-6. In calculating the excess pore pressure ratio r_u, the final vertical position of the pore pressure instrument was used for accuracy. There was speculation regarding their during-event position due to the shallow placement of the sensor and likely disturbance due to unexpected full liquefaction during dynamic A. Figure 3-11 schematically illustrates the observed sand boil locations following dynamic A. Note that PP1 and PP5 were very close to the edges of two of the larger sand boils that occurred during this event, and therefore, it is believed they moved during this event. This speculation of movement of the pore pressure instruments is confirmed by the calculation of the r_u values at complete liquefaction during dynamic A (Table 3-7).

Table 3-6. Initial and final vertical positions of pore pressure instruments

Instrument	Initial depth (inch)	Final depth (inch)
PP1	5.1	9.1
PP2	33.2	35.0
PP3	61.8	58.9
PP4	32.7	35.4
PP5	8.3	11.5

Figure 3-11. Schematic of sand boils following input motion dynamic A

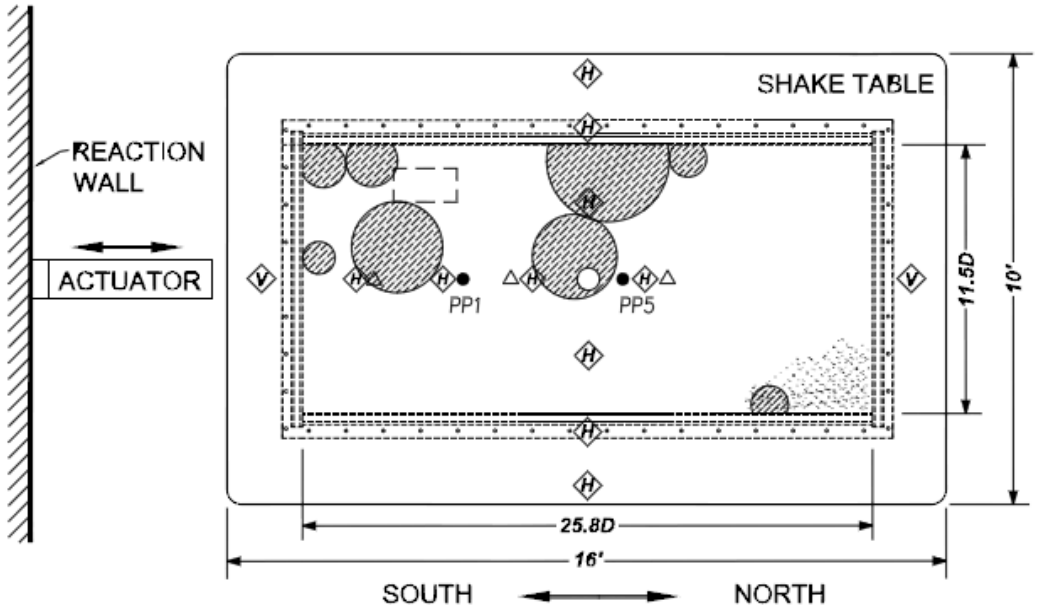

Figure 3-11: Shaded circles and arcs denote locations of sand boils.

Table 3-7. Dynamic A: Initial and Peak μ and r_u

Instrument	Initial μ_o (psi)	Peak μ (psi)	Final σ'_v (psi)	r_u (%)
PP1	0.18	0.49	0.31	100
PP2	1.20	2.50	1.26	103
PP3	2.23	4.33	2.14	98
PP4	1.18	2.55	1.27	107
PP5	0.30	0.68	0.39	97

Dynamic A pore pressures indicate that full liquefaction along the soil column (to the lowest-most measurement of PP3) occurred. Subsequently after shaking, significant pore pressure dissipation was observed prior to static A. Calculations for excess pore pressure ratio r_u use these initial pore pressure values in Table 3-7 for Equation 3.1.

Following the impermeable layer placement, dynamic B was successful in maintaining elevated pore pressures, as observed in Figure 3-13, where PP1 and PP5 are at an r_u of between 16-23% at the start of static B. In Table 3-8, Sensors PP2 and PP4 were elevated to approximately 25-28%, which dissipated to approximately 5% prior to static B. Calculations for excess pore pressure ratio r_u test series B use the initial pore pressure values in Table 3-8 for Equation 3.1.

Figure 3-12. Pore pressure time history for Day 1 (dynamic A and static A)

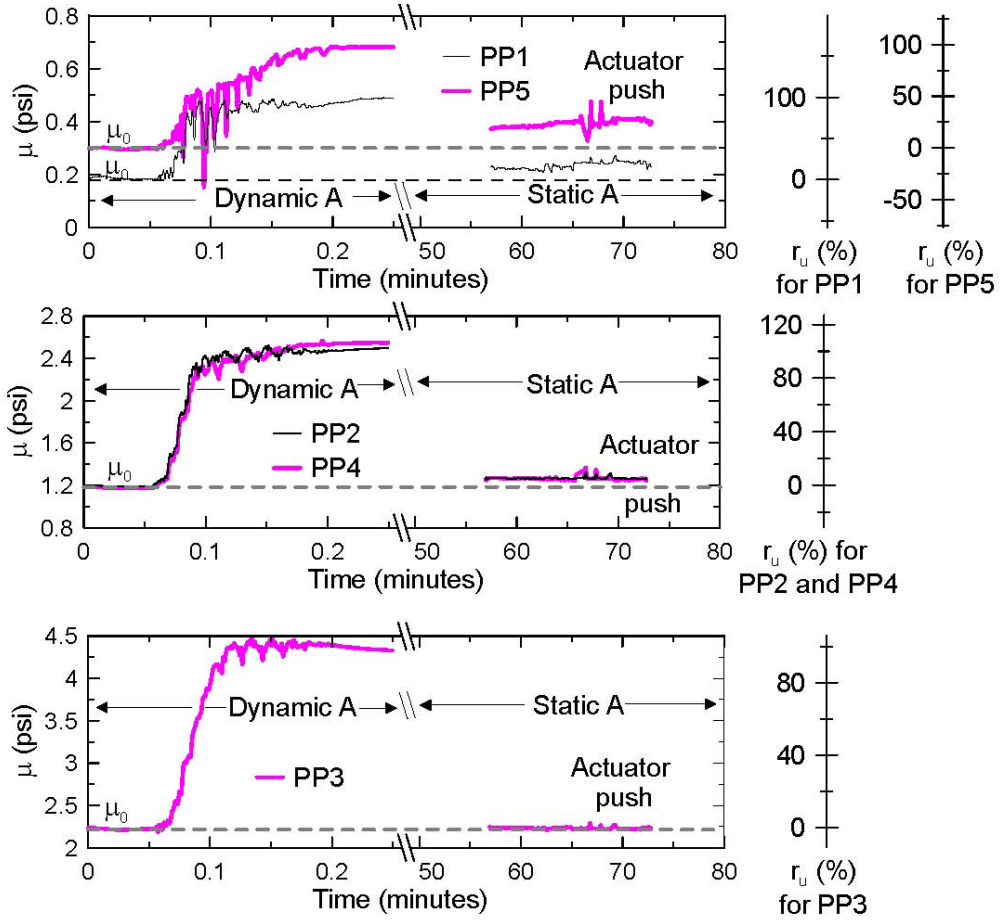

Table 3-8. Dynamic B: Initial and Peak μ and r_u

Instrument	Initial μ_o (psi)	Peak μ (psi)	Final σ'_v (psi)	r_u (%)
PP1	0.19	0.33	0.31	43
PP2	1.25	1.61	1.27	28
PP3	2.20	2.56	2.16	17
PP4	1.29	1.60	1.29	25
PP5	0.40	0.54	0.40	35

Pore pressures from event C indicate that the upper layer did achieve an excess pore pressure, which is shown in Table 3-9. Excess pore pressures for dynamic C are based on initial values from dynamic B, since these tests occurred sequentially on the same day. The initial pore pressures shown in Table 3-9 merely illustrate that excess pore pressures have not fully dissipated at the beginning of dynamic C. Because of the residual pore pressures present at the beginning of dynamic event C, calculations for excess pore pressure ratio r_u (for test series C) use the initial pore pressure values in Table 3-8 for Equation 3.1. Vertical effective stresses for the sensor locations are

Figure 3-13. Pore pressure time history for Day 2 (dynamic B and static B)

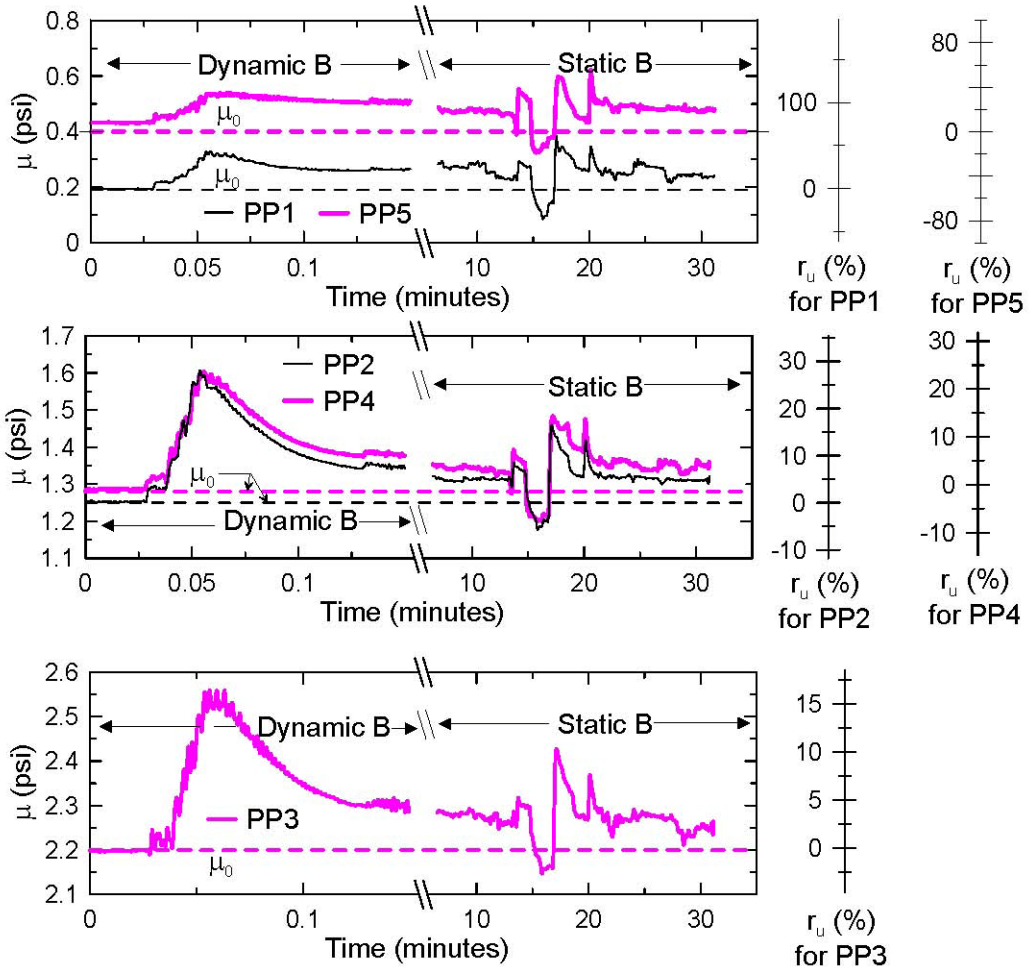

slightly changed from event B because of increasing density of the soil and decreasing depth of the instruments due to settlement. Sensors PP1 and PP5 at the upper layer are shown to have achieved full liquefaction at peak μ, while PP2 and PP4 are in the range of 42-44%, and PP3 is at 25% r_u. For static C, the range of r_u for PP1 and PP5 is 15-20%; for PP2 and PP4, it is 4-5%; and for PP3, it is 3%.

Table 3-9. Dynamic C: Initial and Peak μ and r_u

Instrument	Initial μ_o (psi)	Peak μ	Final σ'_v (psi)	r_u (%)
PP1	0.23	0.60	0.30	119
PP2	1.30	1.83	1.27	42
PP3	2.25	2.78	2.16	25
PP4	1.33	1.90	1.28	44
PP5	0.48	0.87	0.39	100

Figure 3-14. Pore pressure time history for Day 2 (dynamic C and static C)

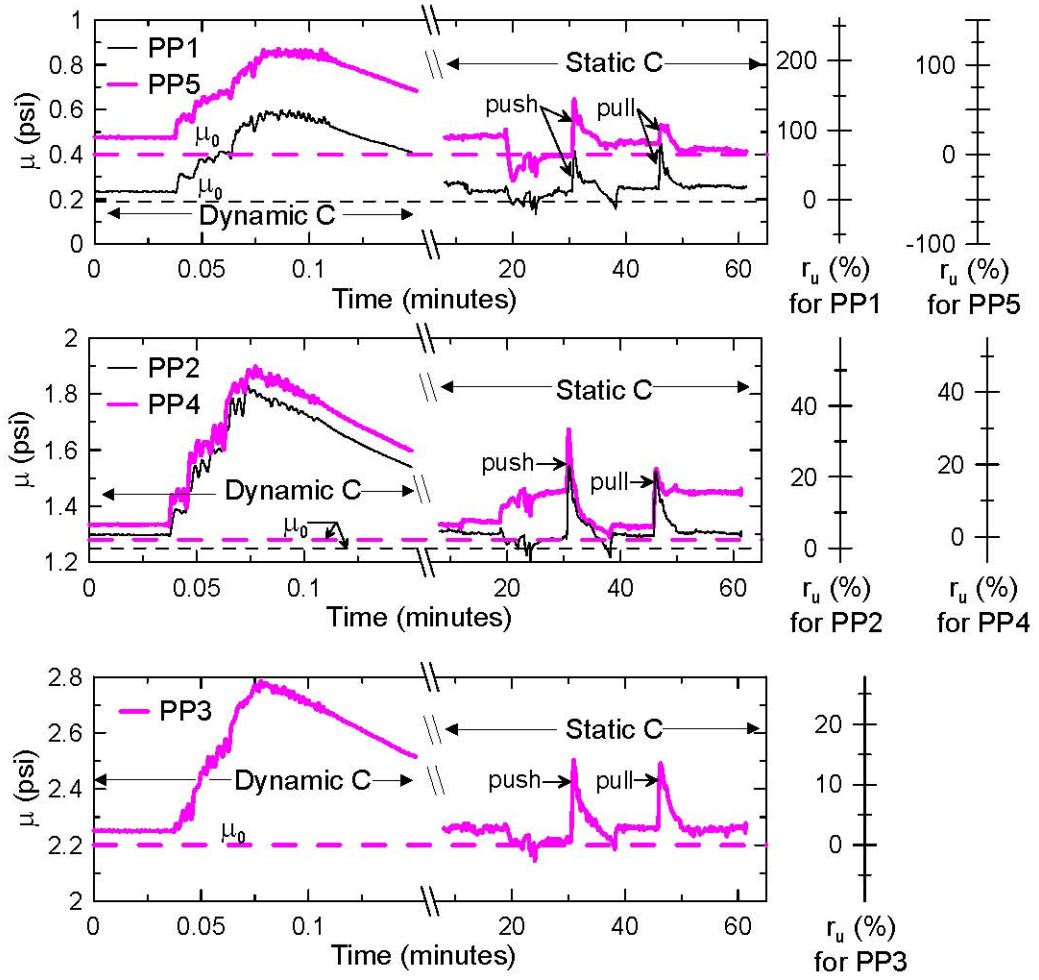

3.2.3 Static Events: Excess Pore Pressure Ratio Time Histories

During the static lateral load tests, a change in excess pore pressure ratio r_u is observed (Figure 3-15) - Figure 3-17. This variation in r_u is caused by movement of the pile and surrounding soil shearing. In these plots, peaks and zero transitions in load and displacements are correlated to changes in r_u. Transducers PP1 and PP5 are placed near the ground surface in the saturated soil layer and are more greatly affected by movement of the pile as well as small disturbances. However, similar peaks and dips in r_u for deeper instruments at PP2, PP4, and PP3 also occur at coincident times, although of lesser magnitude. This behavior is also observed for static tests B and C.

Table 3-10 summarizes the excess pore pressure ratio r_u for static A just before the steel pile was loaded by the actuator and at the peak excess pore pressure. The change in r_u for static A is seen in the time history plot in Figure 3-15. The pile is pushed toward the near field pore pressure transducers and away from the far field pore pressure transducers. Noticeable differences in r_u are observed in PP4 and PP5 when the pile starts to move, where a dip occurs in PP5 and a jump occurs in PP4. One may conjecture that water is moving away from the region of PP5 and possibly moving towards PP4 (which is directly below PP5). During the plateau when 0.8 inches displacement is held, an increase and decrease in r_u is observed to varying degrees for all pore pressure instruments. As the pile returns to zero displacement, a small increase in r_u is produced for all pore pressure instruments except PP4.

Motion of the pile appears to cause the excess pore pressure ratio to change during static loading, yet neither the direction of the pile loading nor the amplitude of the pile loading result in a consistent trend. This behavior is discussed further for static test B. Data from static B and C present a more pronounced change in excess pore pressure ratio r_u due to the larger amplitudes of displacements applied.

Table 3-10. Static A: Initial and Peak μ_o and r_u

Instrument	Initial μ_o (psi)	Initial r_u (%)	Peak μ (psi)	Peak r_u (%)
PP1	0.23	15	0.27	29
PP2	1.28	6	1.33	10
PP3	2.25	1	2.29	3
PP4	1.26	6	1.37	15
PP5	0.37	19	0.48	45

The magnitude of this increase roughly tripled the r_u values for all sensors, with the largest r_u value estimate as 62% for the near surface PP1 (Table 3-11). Static test B imposed displacement towards the far field pore pressure transducers at the south end of the box. While approaching and holding the target displacement, all pore pressure transducers measured a reduction in pore pressure and consequently a reduction in r_u, up to a time of approximately 300 seconds. Upon unloading and returning to zero displacement beyond 300 seconds (movement towards the north end of the box), the opposite occurred, namely pore pressure measurements and consequently r_u increased (Table 3-11 and Figure 3-16). The reductions in r_u may be caused by water flowing into a gap (or loose soil) on the trailing side of the pile. Although it would be expected that water would flow upwards and out of the soil, the impermeable layer would inhibit upward flow.

Water may instead flow into the trailing side of the pile and temporarily reduce pore water pressure. Increases in μ, and consequently r_u, when the pile is unloaded and moved toward zero may be due to water is being squeezed out of the loosen soil on the trailing side of the pile and back into the saturated soil, which then reaches a limit.

Table 3-11. Static B: Initial and Peak μ_o and r_u

Instrument	Initial μ_o (psi)	Initial r_u (%)	Peak μ (psi)	Peak r_u (%)
PP1	0.27	23	0.39	62
PP2	1.31	4	1.46	16
PP3	2.28	4	2.43	11
PP4	1.34	5	1.48	15
PP5	0.46	16	0.62	55

Figure 3-15. Excess pore pressure ratio histories compared with the load and displacement histories for static test A

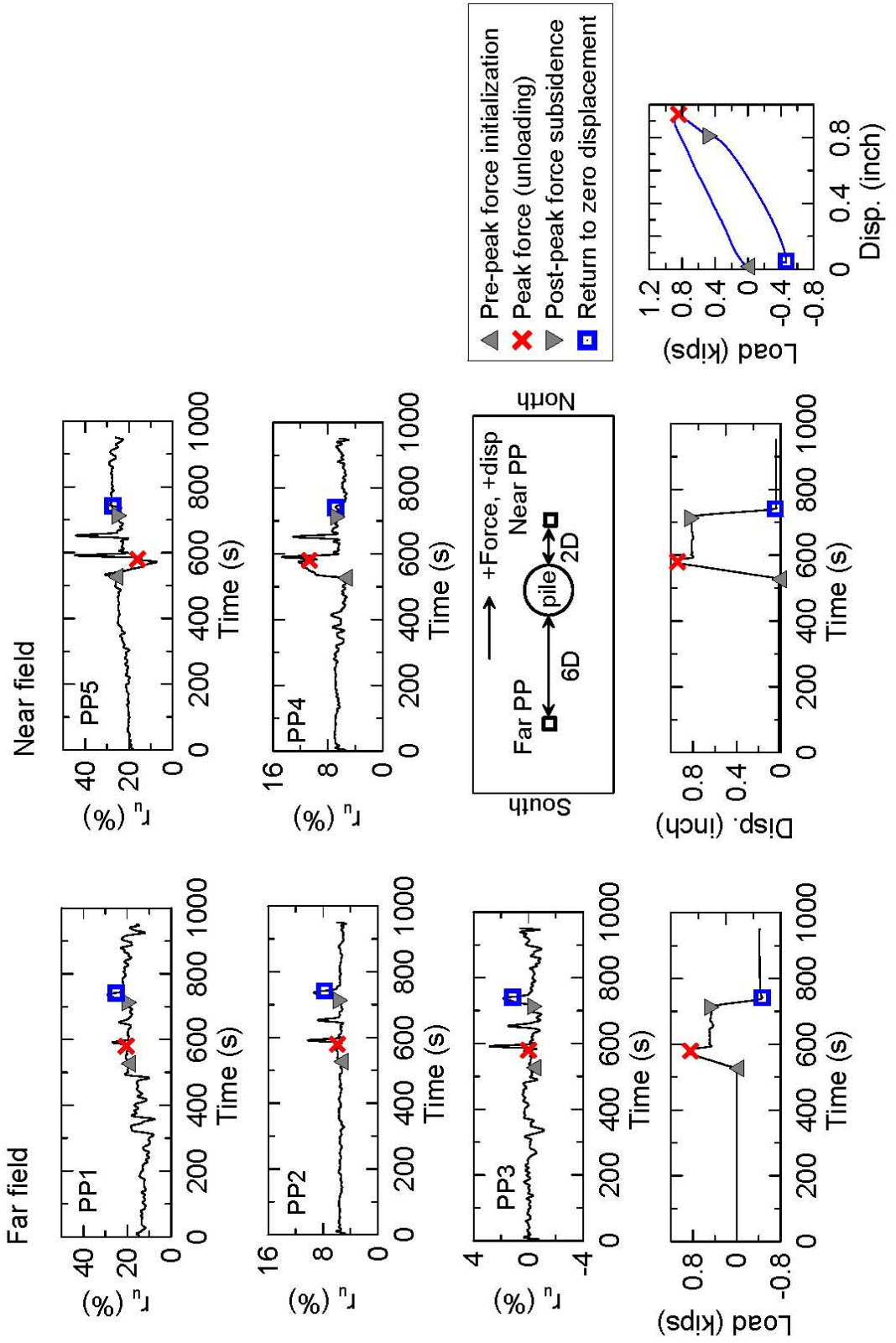

Figure 3-16. Excess pore pressure ratio time histories compared with the load and displacement histories for static test B

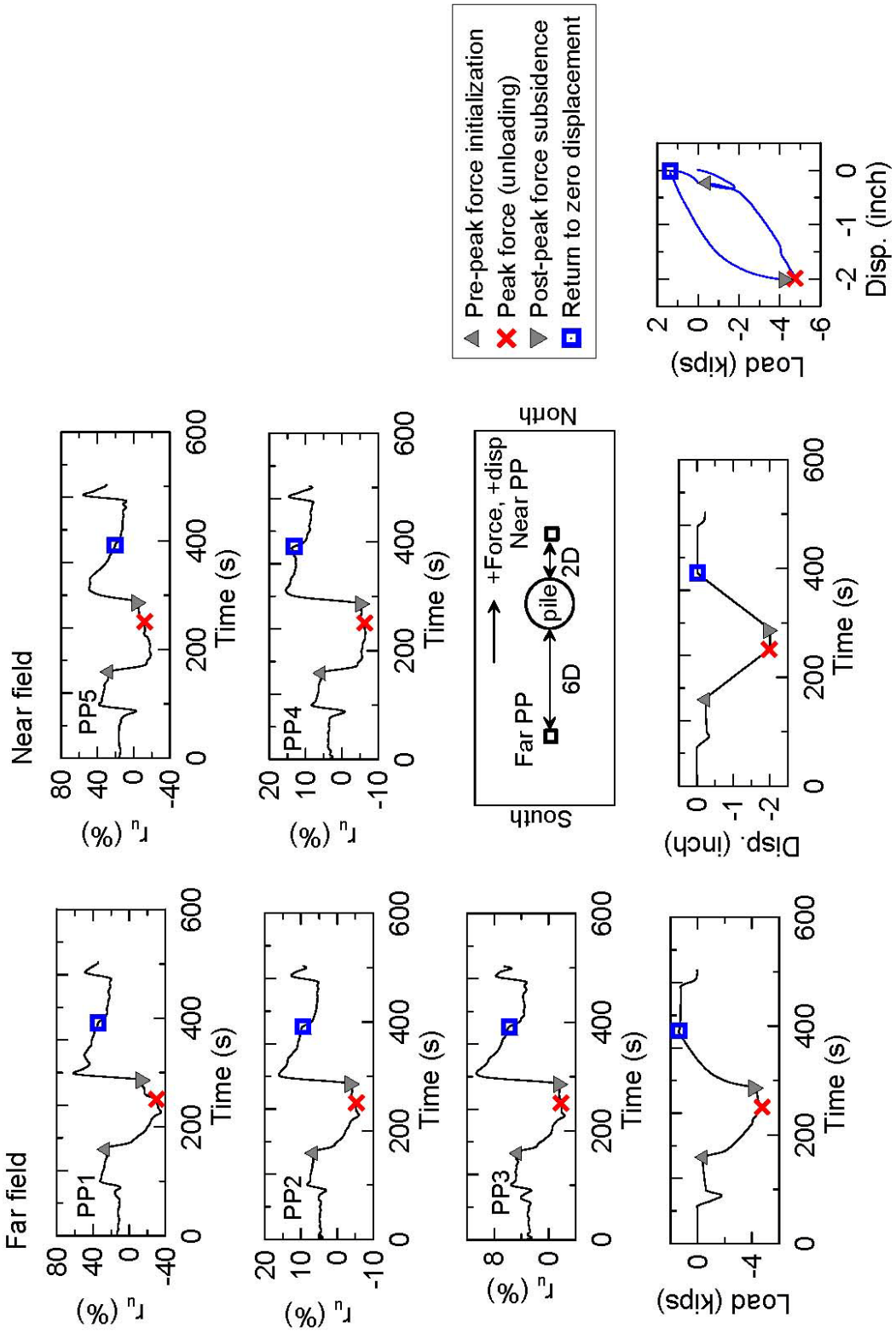

The pore pressure measurements which result during static test C are consistent with those of static test B (Table 3-12 and Figure 3-17). For static test C, however, a full push and pull to peak displacements are invoked on the pile. Nonetheless, rises and drops in μ are consistent with reversals in displacement, and presumably at each significant increase in μ, water is being forced out of the gap (and loose soil) on the formerly trailing side of the pile and returned to the surrounding soil. It should be noted that local shearing may also contribute to apparent pore pressure fluctuations.

Table 3-12. Static C: Initial and Peak μ_o and r_u

Instrument	Initial μ_o (psi)	Initial r_u (%)	Peak μ (psi)	Peak r_u (%)
PP1	0.24	15	0.46	86
PP2	1.31	4	1.54	23
PP3	2.26	3	1.67	14
PP4	1.34	5	1.67	30
PP5	0.48	20	0.65	63

Figure 3-17. Excess pore pressure time histories compared with the load and displacement histories for static test C (landscape)

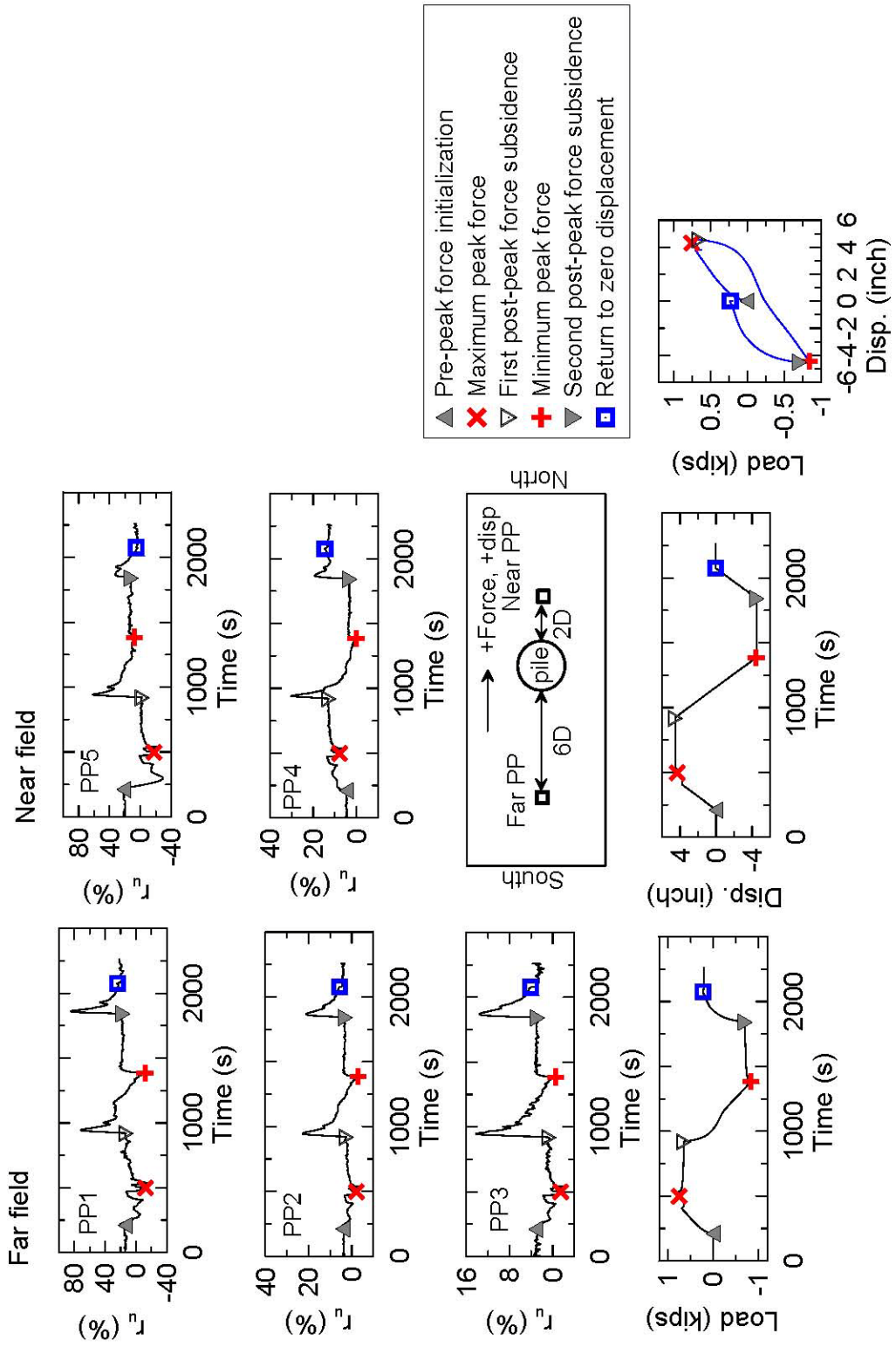

A summary of the initial and peak r_u values is provided in Figure 3-18. Direct comparison via these scatter plots supports the contention that the near surface soil movement and (potential) shearing of the soil most affect the variation in μ and hence r_u, as the change in r_u at greater depths is fairly insignificant. It should be noted that in subsequent presentation of data, reference is made to the initial r_u values. These plots provide important evidence of the sensitivity in pore pressures due to soil movement, particularly in the near surface regions, which are the zones most important to lateral pile response.

Figure 3-18. Profile of initial and peak r_u versus depth for static tests

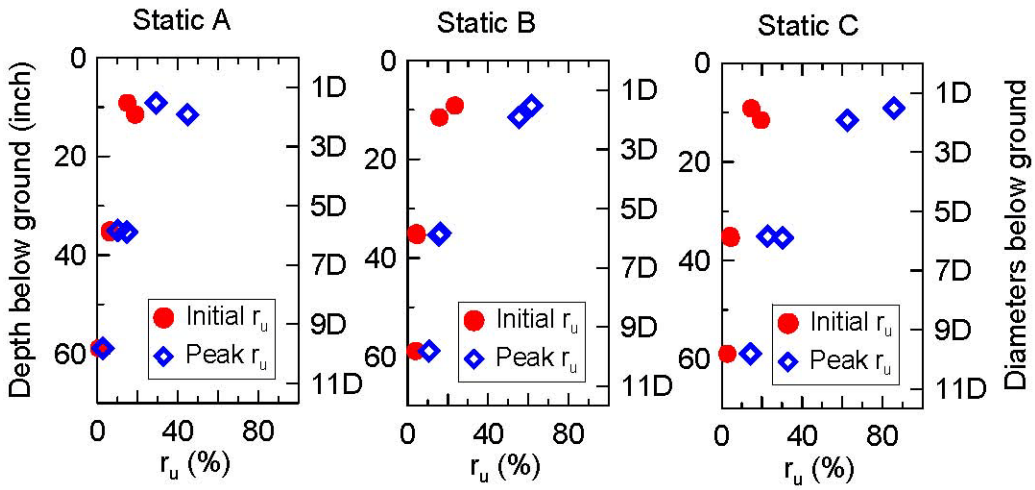

3.2.4 Accelerations of the Saturated Soil Layer

Acceleration histories obtained within the soil layer are presented in Figure 3-19 - Figure 3-21. These plots are arranged in accordance with the sensors' locations within the model. Namely, input acceleration from the shake table is shown in the bottom-most plot; while plots above this show the acceleration histories within the soil layer, with the top-most plots being those near the surface.

The acceleration histories demonstrate approximately consistent behavior at a given elevation within the model, indicating boundary effects were minimized and supporting the contention that the model behaved in the intended shear mode. The vertical distribution of acceleration during dynamic test A clearly indicates the onset of full liquefaction as evident in the period elongation due to pronounced softening of the soil, which occurred at about 7 seconds. In contrast, the acceleration histories support the observed pore pressures for dynamic tests B and C, which presented lower levels of r_u < 100%, which are closer to the intended target r_u values.

In general, the bottom-most acceleration histories have a magnitude that is lower than the table input ground motion. This may be due to lack of full adherence of the liner and soil to the box base and hence introduced minor flexibility, which may reduce transfer of input acceleration slightly. With decreasing depth, the acceleration is amplified for dynamic B and C and generally follows the shape of the input.

Peak uncorrelated acceleration versus depth in Figure 3-22 indicate that accelerations are in general amplified near the ground surface. Acceleration amplification is on the order of 1.5 times the input motion for dynamic tests B and C, while minor de-amplification occurs for the r_u = 100% condition of dynamic A. These observations are consistent with expected behavior of soil columns under full and partial liquefaction.

Figure 3-19. Soil accelerations measured during dynamic A

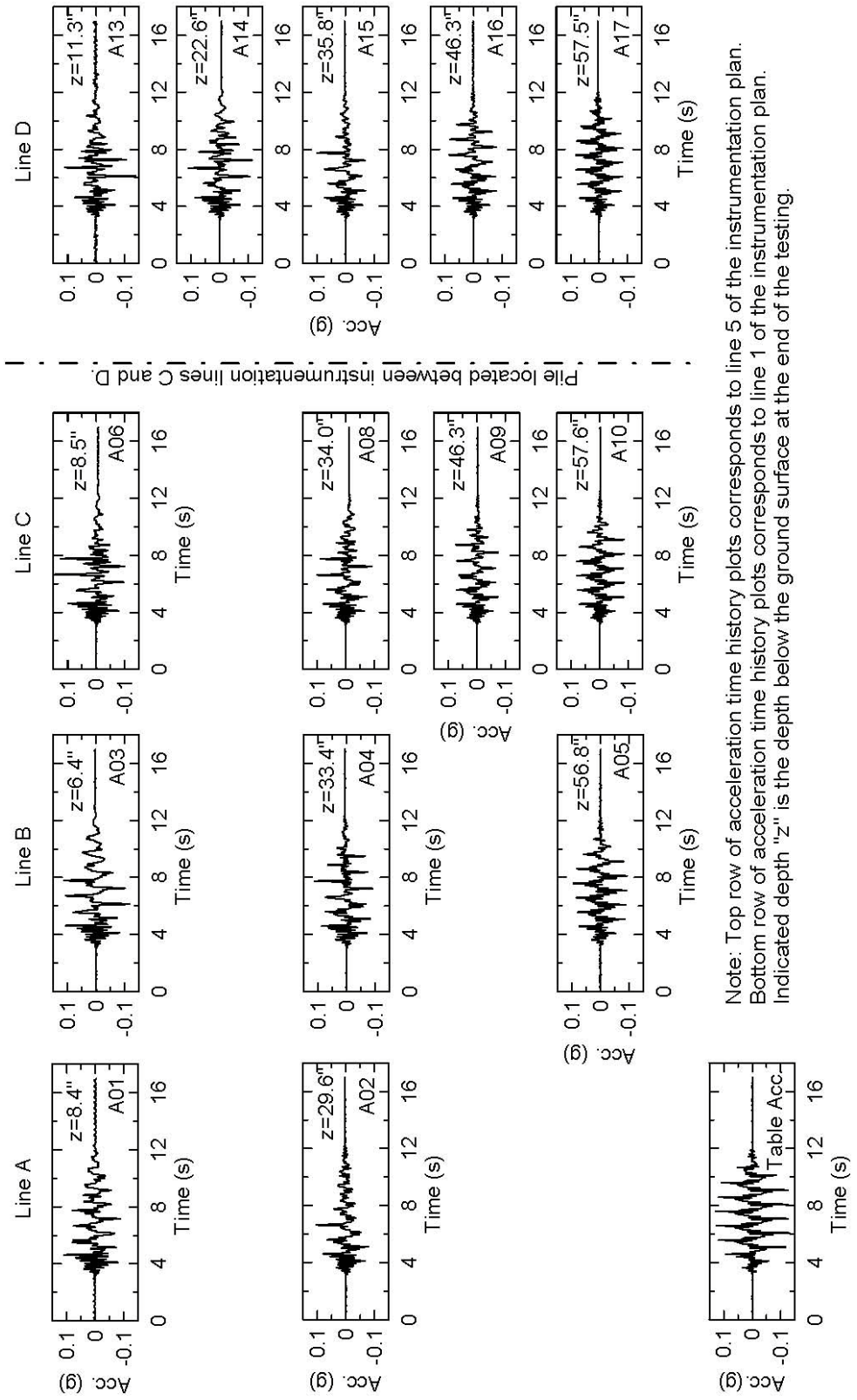

Figure 3-20. Soil accelerations measured during dynamic B

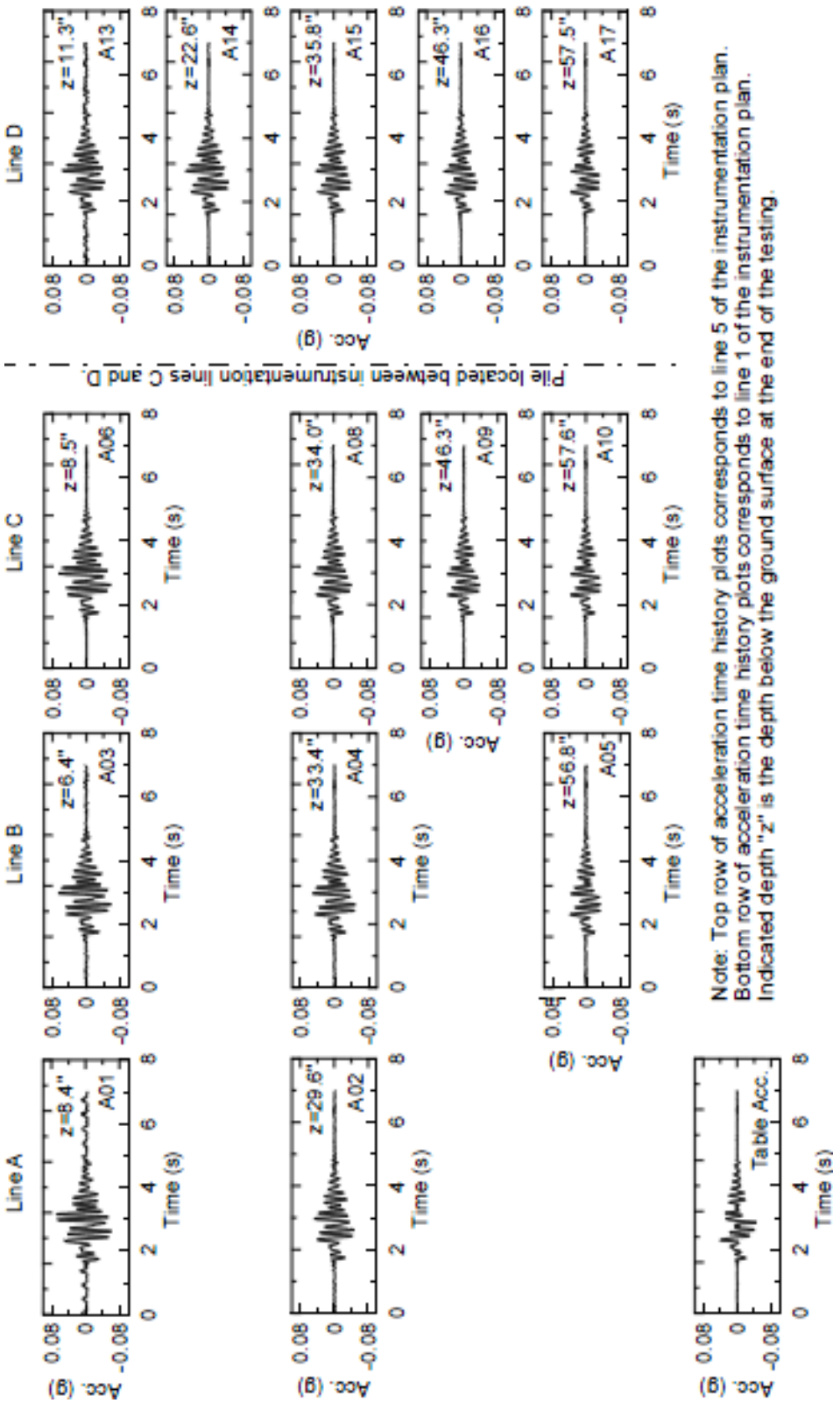

Figure 3-21. Soil accelerations measured during dynamic C

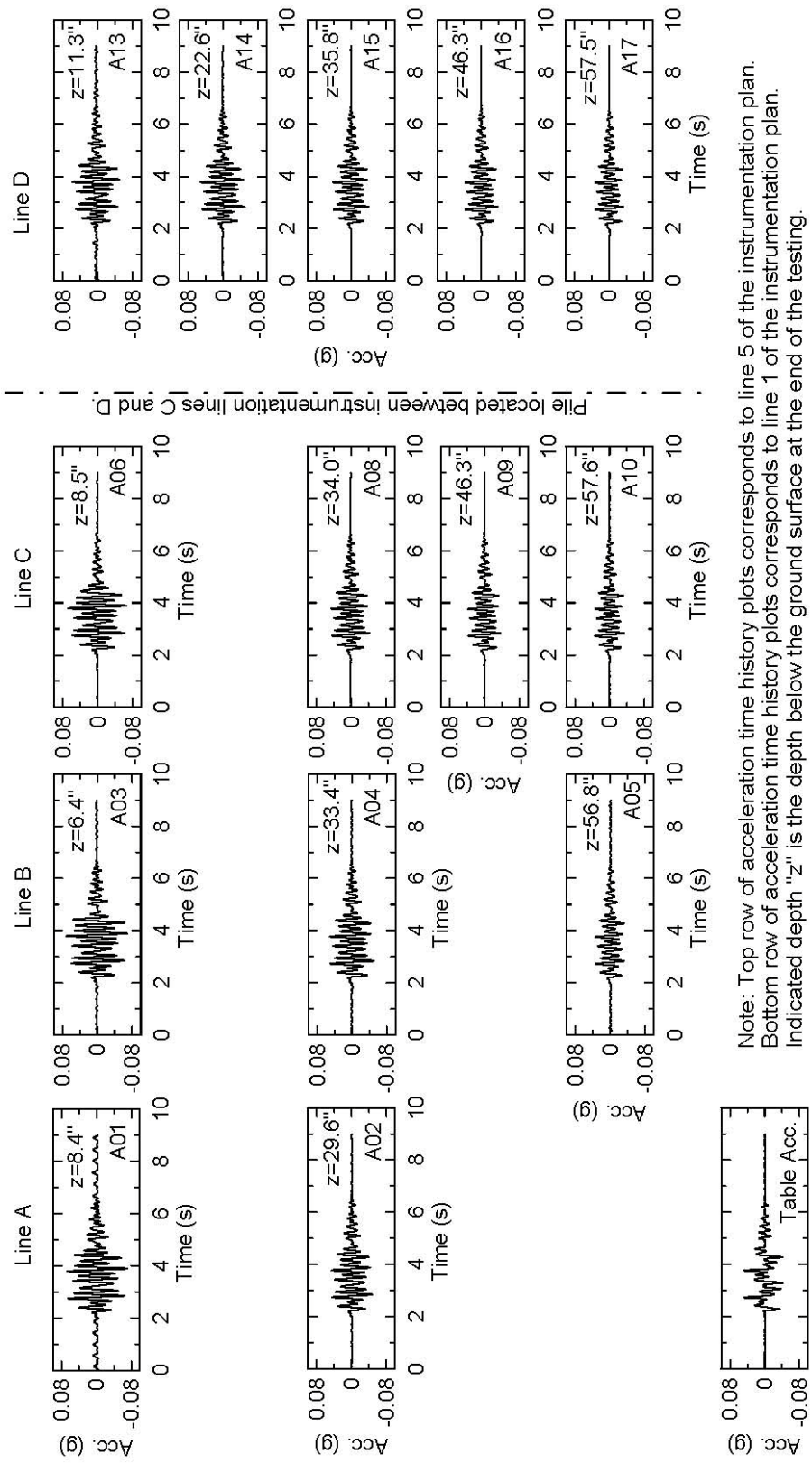

Figure 3-22. Maximum absolute acceleration profile of dynamic A, B, and C

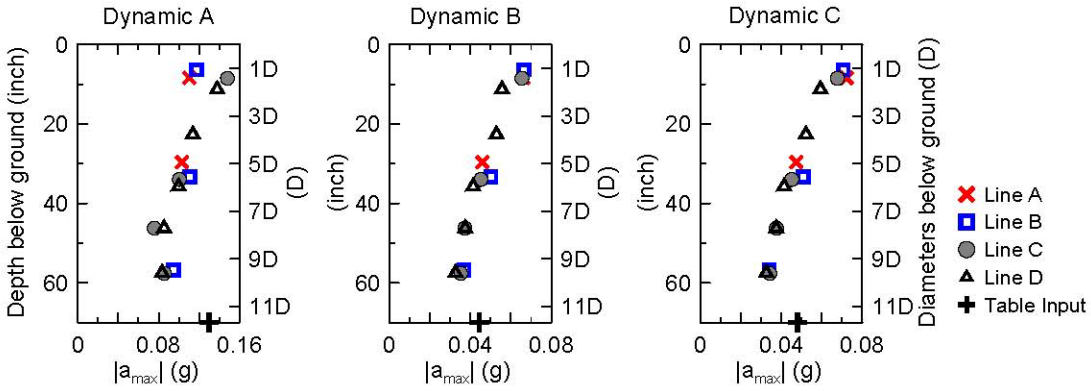

Figure 3-22: accelerations are uncorrelated, i.e. may occur at different times

3.2.5 Static Events: Actuator Load versus Displacement

The piles were loaded under displacement control to the aforementioned targets. The actuator load and displacement were recorded for the static portion of each event (Figure 3-23). To minimize disturbance at the face of the pile, the pile was alternatively pushed then pulled between dynamic shakes. Static A was a push in the northward (positive) direction, while static B was a pull in the southward (negative) direction. Static C was a combined push northward and a pull southward. Each plot of load versus displacement indicates nonlinear behavior of the soil-pile system. Additionally, each plot shows a changing stiffness in the system during each separate push or pull. The final push/pull (static C) needed much less force to push the pile further than the previous static pull (static B). Since pile strains remained elastic, the reduction in strength and associated nonlinear load-displacement behavior of the system is attributed to capacity mobilization of the surrounding soil.

Figure 3-23 provides detailed discretization and analysis of the loading and unloading characteristics observed during static A, B, and C. Tangent stiffnesses for the linear regions of the load-displacement curves are indicated by the arrows and parameterized with “k” labels. Figure 3-24 overlays the three static push test results. Regression is performed to estimate the tangent stiffness values identified in Figure 3-23 (Table 3-13).

Observing the data in Table 3-13, one notes that static B response is stiffer than static A, although both were conducted on “virgin” faces of the pile. An impermeable topping layer was placed following test series A to minimize rapid pore pressure dissipation. This likely resulted in the stiffer response of the soil-pile system for static B. Static C behavior is noted to be much softer than both static tests A and B, as both faces of the pile have been loaded. In addition, following static test B, the impermeable layer has been cracked; therefore, its stiffness to the system will have been diminished, and also three phases of dynamic base shaking have been imposed on the soil-pile model.

Figure 3-23. Lateral load versus displacement at actuator location for static tests A, B, and C

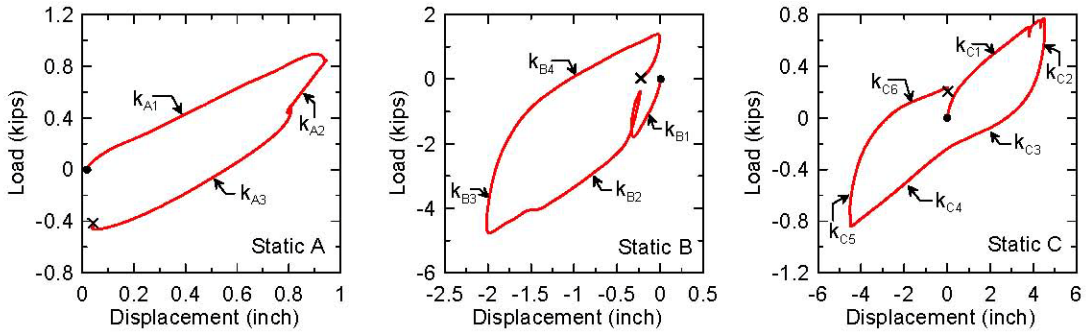

Figure 3.23: Closed "o" denotes the beginning of the test; "x" denotes the end of the test.

The largest value of stiffness occurs during test static B when the actuator starts at the onset of loading and upon the pile's return to its initial displacement (k_{B1} and k_{B3}). Small regions of large stiffness (k_{C2} and k_{C5}) also occur during static C immediately upon unloading in both push and pull directions. The soil-pile system quickly softens, however, indicating the large unloading stiffness is due to gap closure. Visible gaps were observed at the ground surface during lateral loading. Comparison of the three static loading tests is provided in Figure 3-24. This direct comparison is useful as it illustrates a few key points:

1. Initial loading of the soil-pile system was largest during the pull cycle of static B. In comparison with static A, this is attributed to the densification that occurred in the prior dynamic shakes, as well as the presence of the newly placed impermeable layer. The softer behavior of static C may be attributed to cracking of the impermeable layer in prior shakes and static loads, prior load history imposed on the soil (at this point both the front and back of the pile have been loaded), and flexibility of the pile base connection.

2. The trend with regard to load amplitudes at peak displacements for each static test may be attributed to similar reasoning described in point 1.

3. The displacement capacity of the soil-pile system, as demonstrated in static C, conducted at an initial r_u = 15-20%, exceeds that of the cantilever fixed base pile estimated yield. This supports the contention that base flexibility must be considered in the modeling of the specimen. The theoretical cantilever yield shear force V_y is 1.7 kips, and the theoretical cantilever yield displacement Δ_y is 3.6 inches.

Figure 3-24. Overlay of lateral load versus displacement for all static tests

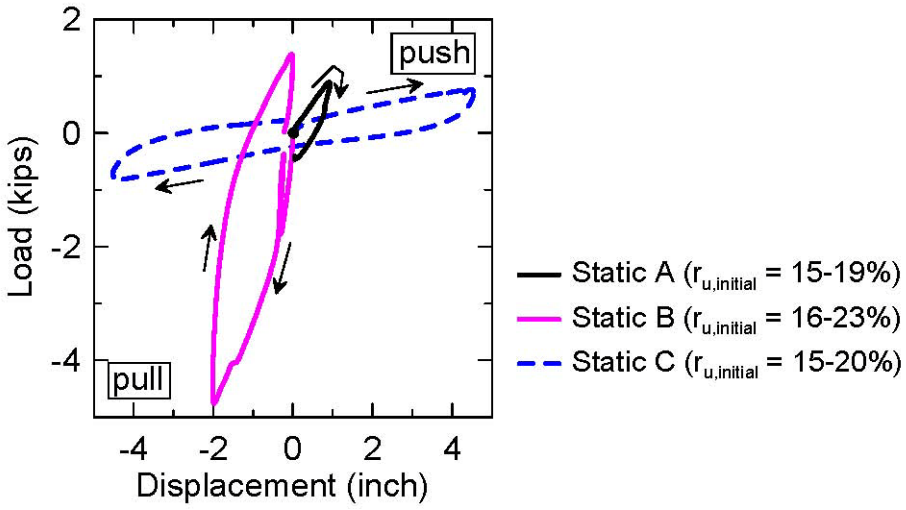

Table 3-13. Tangent stiffness for static tests

Test Name	Static A	Static B	Static C
k_1 (kip/in)	0.97	5.54	0.14
k_2 (kip/in)	2.61	2.04	1.55
k_3 (kip/in)	1.22	10.7	0.09
k_4 (kip/in)	–	1.73	0.14
k_5 (kip/in)	–	–	1.52
k_6 (kip/in)	–	–	0.11

3.2.6 Actuator Measured Response and Strain Gage Calculated Response of the Pile

To rationalize the differences in the strain gage calculated response, a comparison is made of the actuator measured response measurements obtained from the pile head (actuator and external displacement transducer) with those obtained using local measurements on the pile, namely the integration and differentiation of the strain gages placed on the pile surface. The former is denoted *actuator measured response*, whereas the latter is denoted *strain gage calculated response*.

The use of strain gage data relies upon elastic beam theory and uses either double integration to obtain the pile displacement or single differentiation to obtain pile shear force. For this experimental setup, the strain gage calculated response more closely reflects the steel pile's true response because it is based on the bending behavior of the pile. As the pile bends, the strain gages elongate, and any accompanying shear forces (V_{strain}) and displacements (Δ_{strain}) at specific locations may be determined. When the displacement of the pile is not due to bending, then the strain gages will not measure this. Because of non-bending related displacements ($\Delta_{additional}$) of the pile, the strain gage calculated response of the pile is not the same as the actuator measured

response. Non-bending displacements are attributed to boundary conditions of the soil-pile set-up.

In this experimental setup, the steel pile was installed into a steel collar by using concrete and two foam inserts. The steel collar (and pile) was bolted to the bottom plate of the laminar soil box. To prevent water from leaking out of the box through the bolt holes, rubber washers (1/8" thick) were also installed below and above the plate (Figure 3-25). From the no-soil push test data, an estimate of the horizontal displacement caused by the aggregate rotation of the pile to collar connection and the collar to bottom plate connection may be made. A summation of the strain gage calculated displacements ($\Sigma\Delta$) from pile bending below the soil, pile bending above the soil, and pile hinging from the base rotation is compared to the measured displacement at the actuator ($\Delta_{actuator}$) in Table 3-14.

Similarly, the actuator measured shear force ($V_{actuator}$) may be considered the sum of shear force from bending (V_{strain}) and shear forces that contribute to elastic rotation of the pile or resistance from cracking of the topping ($V_{difference}$) (see Table 3-15). This summation of shear forces is supported by data from the no-soil push test, where a portion of the actuator measured shear force caused bending in the steel pile and another portion caused the elastic rotation of the pile. Depending on the individual static test, it is believed that the summation of different mechanisms is contributing to the global shear force and displacement.

From this analysis, the following comments may be made:

1. In static test A, the steel pile, embedded in a saturated loose soil, was pushed in the northward direction. The actuator measured displacement ($\Delta_{actuator}$) of the pile is 0.95 inches. From double integration of the curvature (which is based on the strain data), a strain gage calculated displacement (Δ_{strain}) of 0.23 inches is obtained. An estimate of the displacement from rotation of the pile, which is calibrated from the no-soil test and from inclinometer measurements, and the displacement of above ground bending of the pile is made ($\Delta_{additional}$). Then, the sum of these two estimated displacement components ($\Delta_{strain} + \Delta_{additional} = \Sigma\Delta$) is taken. The difference in displacement between the measured ($\Delta_{actuator}$) and calculated ($\Sigma\Delta$) values is essentially zero. Since the no-soil push test was used for calibration, $\Delta_{difference}$ equal to zero is reasonable because both this test and the no-soil push test were pushed by the actuator to almost 1 inch. Additionally, the strain gage calculated shear forces observed in static test A are proportionally consistent with shear forces observed in the no-soil push test.

2. In static test B, the steel pile was pulled in the southward direction. This static test was the first lateral push following the placement of the impermeable layer which was placed to minimize pore pressure dissipation. A calculation of the strain gage calculated displacement (Δ_{strain}) and an estimate of the displacement due to elastic rotation ($\Delta_{additional}$) are again made, and the summation of the two ($\Sigma\Delta$) is compared to the displacement of the actuator ($\Delta_{actuator}$). The difference between these two ($\Delta_{difference}$) is 0.05 inches. Although the displacements may be reconciled, the shear forces are more difficult to reconcile due to the impermeable layer shear resistance. A residual shear force ($V_{difference}$) of 3.93 kips remains after subtracting out the shear force due to bending at the ground surface (V_{strain}) from the global shear force ($V_{actuator}$). After the pull on the pile, visual observations during testing revealed very small cracks in the surface of the

topping, separation of the topping from the sides of the geotechnical liner, and separation and settlement of the topping around the steel pile. This large actuator measured shear force is reasonable considering the minor damage to the impermeable layer. Note that only a thin width of the intact impermeable layer pushing against the pile (less than 1" width) would be needed to provide the $V_{difference}$ resulting in this push.

3. In static test C, the steel pile is pushed to the north and then pulled to the south. Since this test occurs after static test B, lower actuator measured shear forces ($V_{actuator}$) are expected and observed. Actuator measured displacement ($\Delta_{actuator}$) of the specimen is taken to an extreme 4.53 inches. This displacement is beyond the yield displacement as based on a theoretical no-soil cantilever assumption. However, during testing, strains in the pile did not surpass the yield strain. Therefore, a large majority of the displacement is actually from elastic rotation of the pile itself. This hypothesis is supported by the amount of displacement and shear force at the ground surface (Δ_{strain} and V_{strain})– neither of which is larger than yield displacement or yield shear force. Again, based on the no-soil calibration data, an estimate of the displacement from the rotation ($\Delta_{additional}$) is calculated. From the tables, it is shown that the differences (push and pull) between the estimated and measured displacements are about 0.49 and 0.57 inches. In this particular test, the pile is displaced far enough that the calibration for displacement is not as good as the previous two tests. Additionally, the bottom plate of the laminar soil box has reached its limit and has begun to ”pull back” at the pile as it bends. This is reflected in the incongruity between the actuator measured shear force ($V_{actuator}$) and the strain gage calculated shear force at the ground surface (V_{strain}). Since the bottom plate of the soil box is providing a restoring force and more bending to the pile, V_{strain} is larger than $V_{actuator}$.

Figure 3-25. Pile to collar connection which is bolted to the bottom plate of laminar soil box

Table 3-14. Measured and estimated displacements at the pile head

Test name	$\Delta_{actuator}$ (inch)	Δ_{strain} (inch)	$\Delta_{additional}$ (inch)	$\Sigma\Delta$ (inch)	$\Delta_{difference}$ (inch)	Comment
A	0.95	0.23	0.72	0.95	0.0	(1)
B	2.02	0.49	1.48	1,97	0.05	(2)
C	4.53	0.81	3.15	3.96	0.57	(3)
C	4.53	0.87	3.17	4.04	0.49	(3)

Table 3-15. Measured and estimated shear forces at the pile head

Test name	$\Delta_{actuator}$ (inch)	Δ_{strain} (inch)	$\Delta_{difference}$ (inch)	Comment
A	0.89	0.38	0.51	(1)
B	4.76	0.83	3.93	(2)
C	0.77	1.15	-0.38	(3)
C	0.84	1.18	-0.34	(3)

3.3 Development of Experimental P-Y Curves

3.3.1 Overview

A key goal of this test program was the back-calculation of p-y curves at a range of initial r_u values. To this end, strain measurements, coupled with boundary conditions, and numerical integration and differentiation are implemented. In the following sections, the procedures used in the numerical processing are described.

3.3.2 Maximum Moment and Curvature Profiles

Strains in the pile were below yield and remained elastic; maximum push refers to northward movement and pull refers to southward movement. The $r_{u,initial}$ reported is for the upper region (z=1.9D) pore pressure measurement locations. Therefore, maximum moment and curvature may be calculated using the recorded strains during testing from Equations 3.2 and 3.3.

$$M(z,t) = \phi EI \tag{3.2}$$

where φ is curvature at a depth z along the pile and time t, I is the moment of inertia, and E is the modulus of elasticity, as determined from material tests.

$$\Phi(z,t) = \frac{\Delta\epsilon(z,t)}{d} \tag{3.3}$$

where $\Delta\epsilon(z, t)$ is the difference in strain between the tension and compression faces of the pile at elevation z and time t, and d is the distance of the outer diameter of the pile, i.e. the gage length

between the strain measurements. Profiles of the maximum moment and curvature along the pile length are shown in Figure 3-26 and Figure 3-27. These profiles show expected trends in terms of zero moment at the pile load application and return to either small moment reversal or approximately zero moment at the pile base. It should be noted that with the addition of the impermeable layer between day 1 and 2, the depth to maximum moment is shifted closer to the ground surface. This is anticipated due to the increase in stiffness provided by the new thin layer.

3.3.3 P-y Curves from Static Tests

Soil resistance and pile displacement p-y curves for the static tests were back-calculated using the moments and curvatures determined in the previous section. At the pile base where no

Figure 3-26. Maximum moment distribution in the pile for static tests A, B, and C

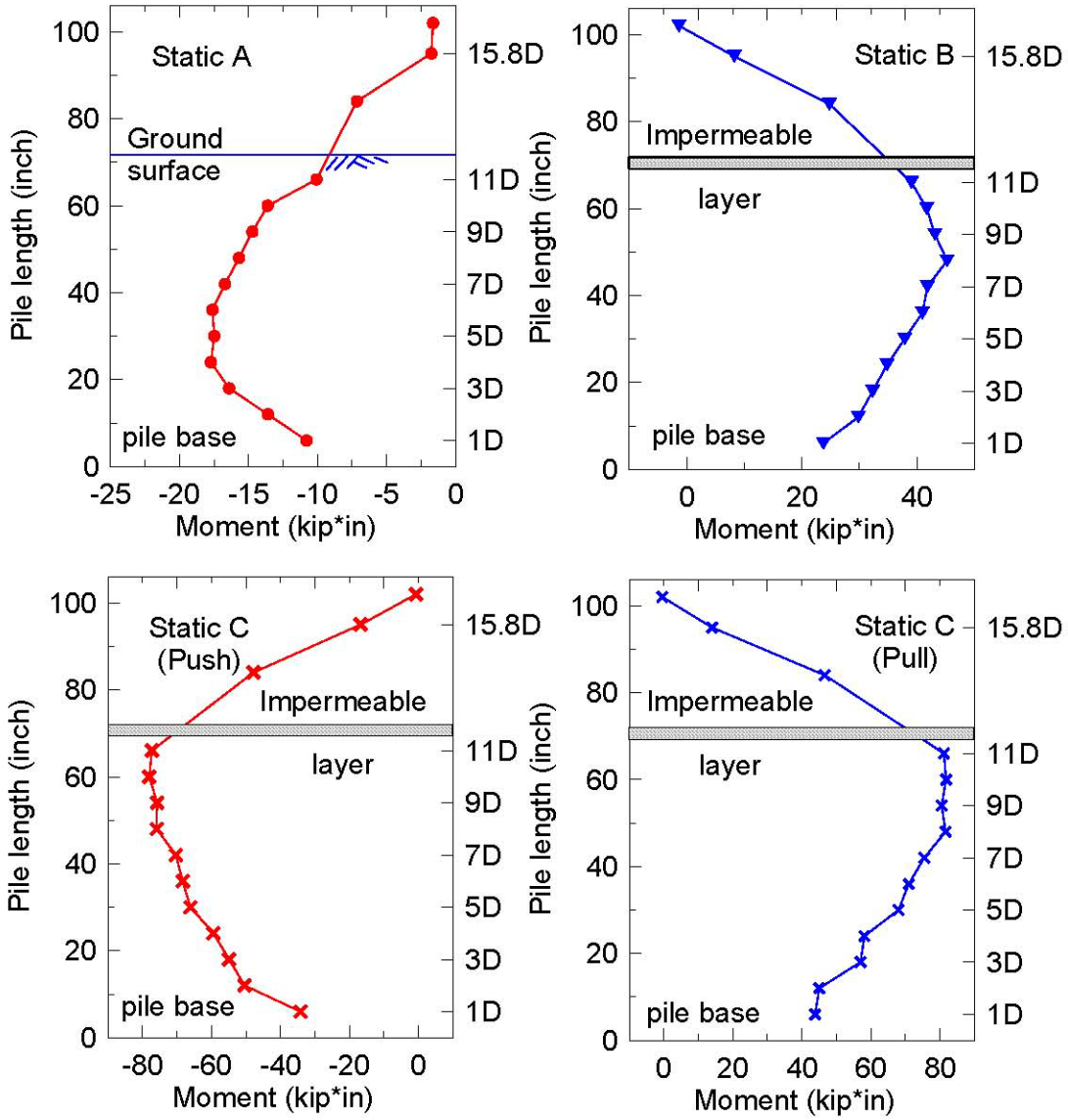

strain data was captured, an estimate was made for the moment at the base. Bending moment of the pile was differentiated with respect to length of the pile to obtain shear force. This shear force was then differentiated with respect to the length of the pile to obtain pressure *p* (Equation 3.4). After each step of the numerical differentiation, a low-pass Butterworth filter was applied to the data to minimize the errors inherent in the differentiation process. Curvature of the pile was integrated twice with respect to the length of the pile to obtain the soil displacement *y* (Equation 3.5). Numerical integration was implemented with the composite

Figure 3-27. Maximum curvature distribution in the pile for static tests A, B, and C

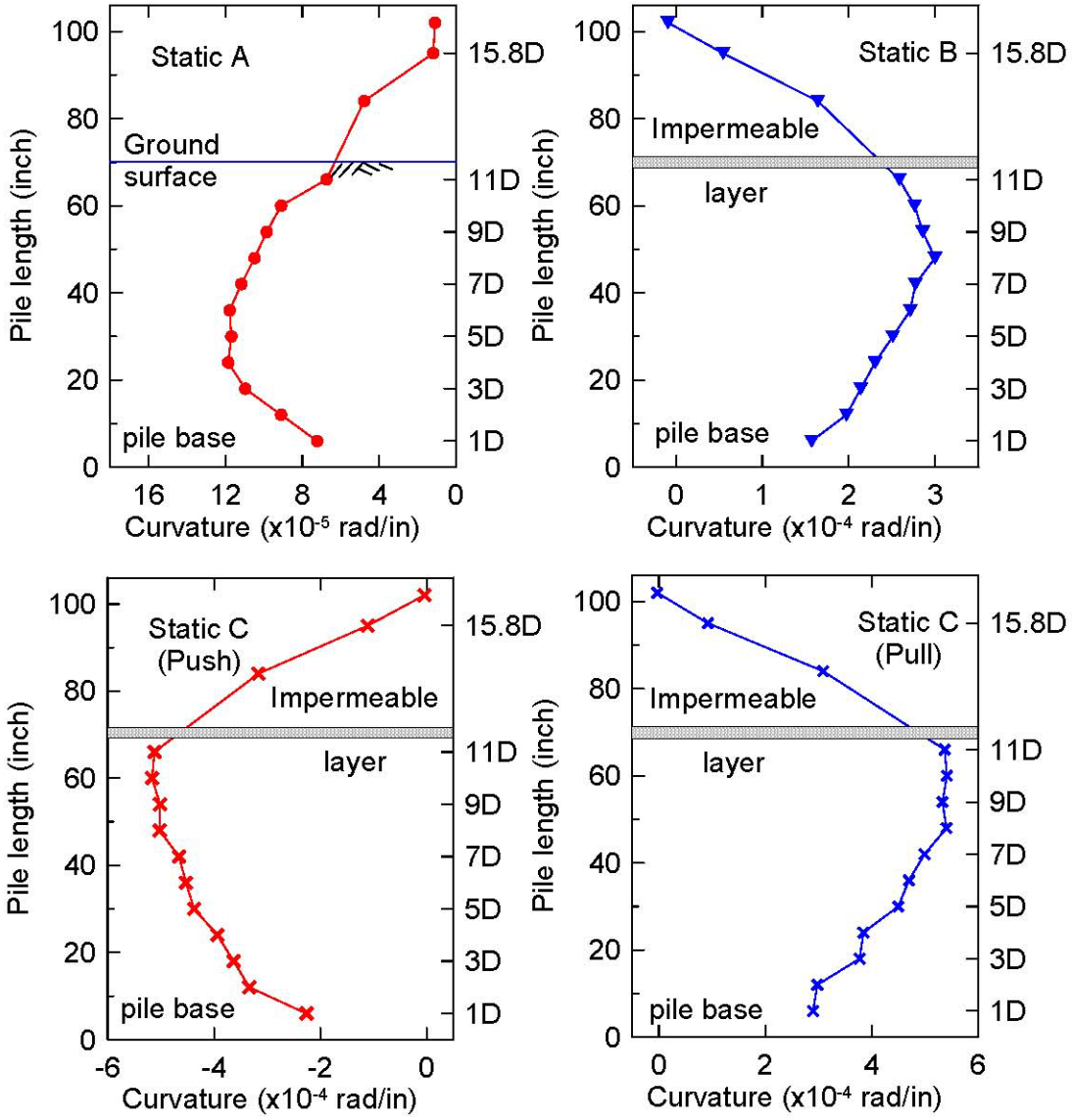

Simpson's rule

$$p(x) = \frac{d^2}{dx^2}(Mdx) \tag{3.4}$$

$$y(x) = \int\int \Phi dx \tag{3.5}$$

A widely accepted recommended practice from the American Petroleum Institute (API) advises the use of a calculated bilinear p-y curve to estimate the soil resistance of piles in saturated soils (API, 1993) with this equation:

$$p = Ap_u tanh(\frac{kH}{Ap_u}y) \tag{3.6}$$

where p is soil resistance, A is a factor to account for cyclic or static loading, p_u is the ultimate bearing capacity at depth H (lbs/in), k is the initial modulus of subgrade reaction (lb/in^3), y is the lateral deflection (inch), and H is the depth (inch). From the same design guidelines, the ultimate bearing capacity p_u is calculated at a given depth H by whichever equation which gives the smaller value of p_u. These two equations are:

$$p_{us} = (C_1H + C_2D)\gamma H \tag{3.7}$$

and:

$$p_{ud} = C_3D\gamma H \tag{3.8}$$

where C_1, C_2, and C_3 are unitless coefficients determined by graphical plots based on the angle of internal friction of the sand (degrees), D is the average pile diameter from surface to depth (inch), γ is the effective soil weight (lb/in^3), and H is the depth (inch). Estimated p-y curves from using the API equation are compared to the experimental results in the following Figure 3-28 - Figure 3-32.

Using the aforementioned methods results in the p-y curves for static tests A, B, and C, as shown in Figure 3-28 - Figure 3-30. With some exceptions, these plots are shown on the same scale and proportional slope from between tests A-C for ease of comparison. The effects of a partial degree of liquefaction is shown in the decreasing stiffness of the p-y curves as the p-y plots move from near the bottom of the soil layer (location #01) to near the top of the soil layer (location #11). For static A, an initial r_u of 15% to 19% was measured near the top of the saturated soil layer, and an initial r_u of 1% was measured near the bottom of the saturated soil layer. For static B, an initial r_u of 16% to 23% was measured near the top of the soil layer, and an initial r_u of 4% near the bottom. Static C had an initial r_u of 15% to 20% near the top and an initial r_u of 3% near the bottom. Likewise, an increasing amplitude of p at the maximum y is observed near the ground surface as anticipated.

Although an inverted S-shaped p-y curve is not apparent in the static A p-y curves, the inverted S-shape becomes more apparent in the static C p-y curves. For static C locations #09, #10, and #11 at near surface locations (the upper 2.7D), the inverted S-shape is clearly evident. This inverted S-shape as characterized by a low initial stiffness and gradual stiffening upon continued displacements. At larger displacements, the p-y curve has the characteristic stiffening of liquefied soils. The static B shows similar behavior to a lesser degree than static C. The inverted S-shaped p-y curve has the potential to surpass the estimated API p-y curve at large displacements and, in fact, does.

Figure 3-31 shows a comparison of all back-calculated p-y curves for static A, B, and C. The limit and slope of the API p-y curves for stable soil is also shown. In general, the p-y curves for these three static tests overlap. At these locations (further up the pile and closer to the ground surface), the slopes of the p-y curves are less than the API p-y curves of stable soil as calculated by methods from the American Petroleum Institute (API, 1993). Soil resistance is shown to exceed the expected strength of the soil (as indicated by the limit of the solid red line) at locations #10 and #11 for static C. Initial experimental stiffness of the p-y curves are decreasing as excess pore pressure ratio r_u increases. At locations #04 and #05 (near the middle of the pile), the slopes of these p-y curves tend to match the slope of the API p-y curve for stable soil. In contrast, at the base of the pile, slopes of the experimental p-y curves are stiffer than the design p-y curves.

From the comparison plots, it may be inferred that near the top of the saturated soil layer, where initial r_u of 15% to 23% occurs, this initial r_u is sufficient to cause a reduction in the soil resistance at small displacements (Figure 3-32). However, this initial r_u (15% to 23%) was not sufficient to cause zero soil resistance at small displacements, which has been recently observed for laterally loaded pile experiments with complete liquefaction. Hardening behavior of the soil resistance at larger displacements is observed.

This particular test series only addresses soil resistance for partially liquefied soils when the laterally loaded pile presses against virgin (or nearly undisturbed) soil. Cyclic loading of the pile was not addressed, and this should be considered in future testing and/or numerical simulations.

Figure 3-28. P-y curves for static A

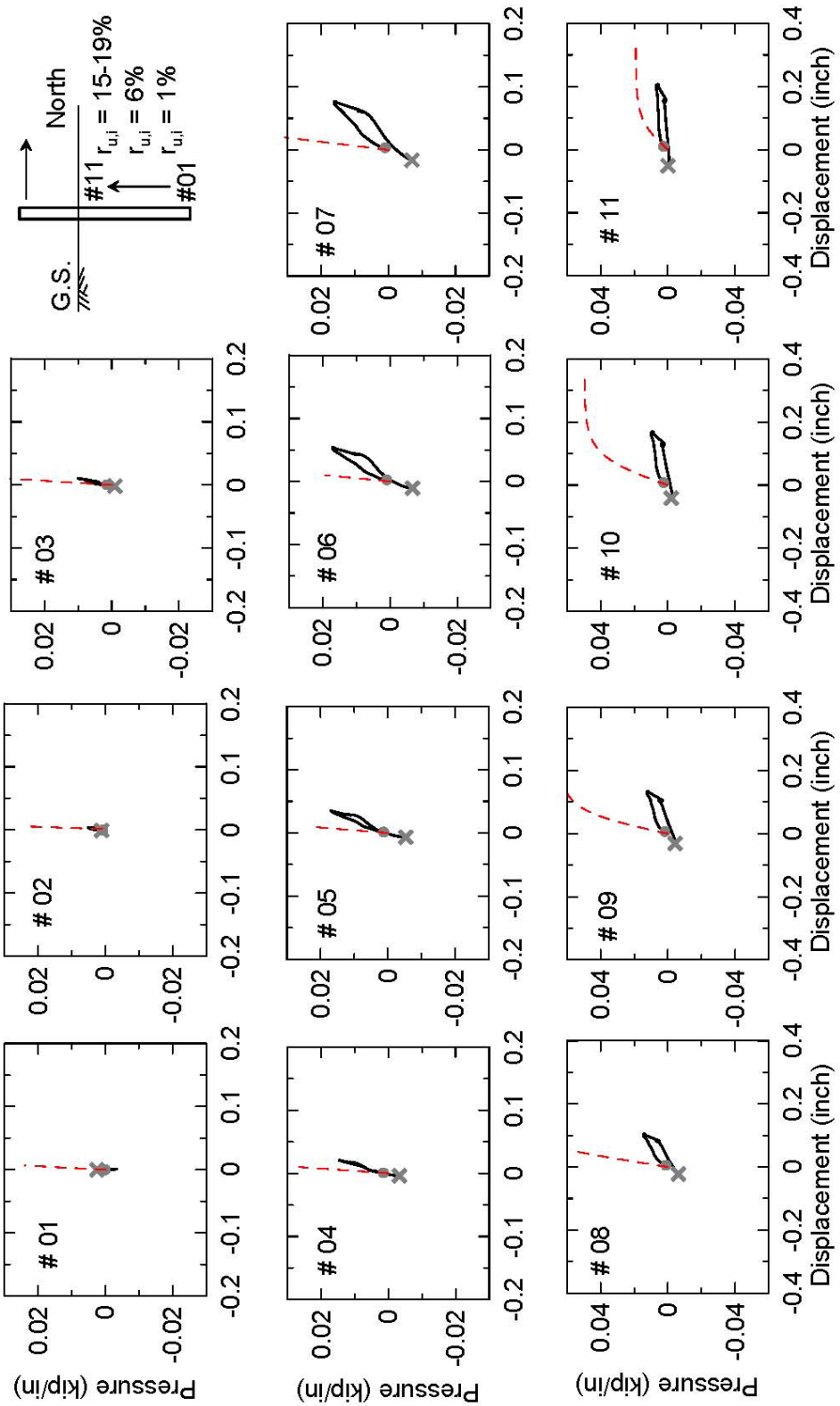

Figure 3-28: Circle denotes beginning of test; "x" denotes end of test. Dashed red line denotes bilinear API p-y curve

Figure 3-29. P-y curves for static B

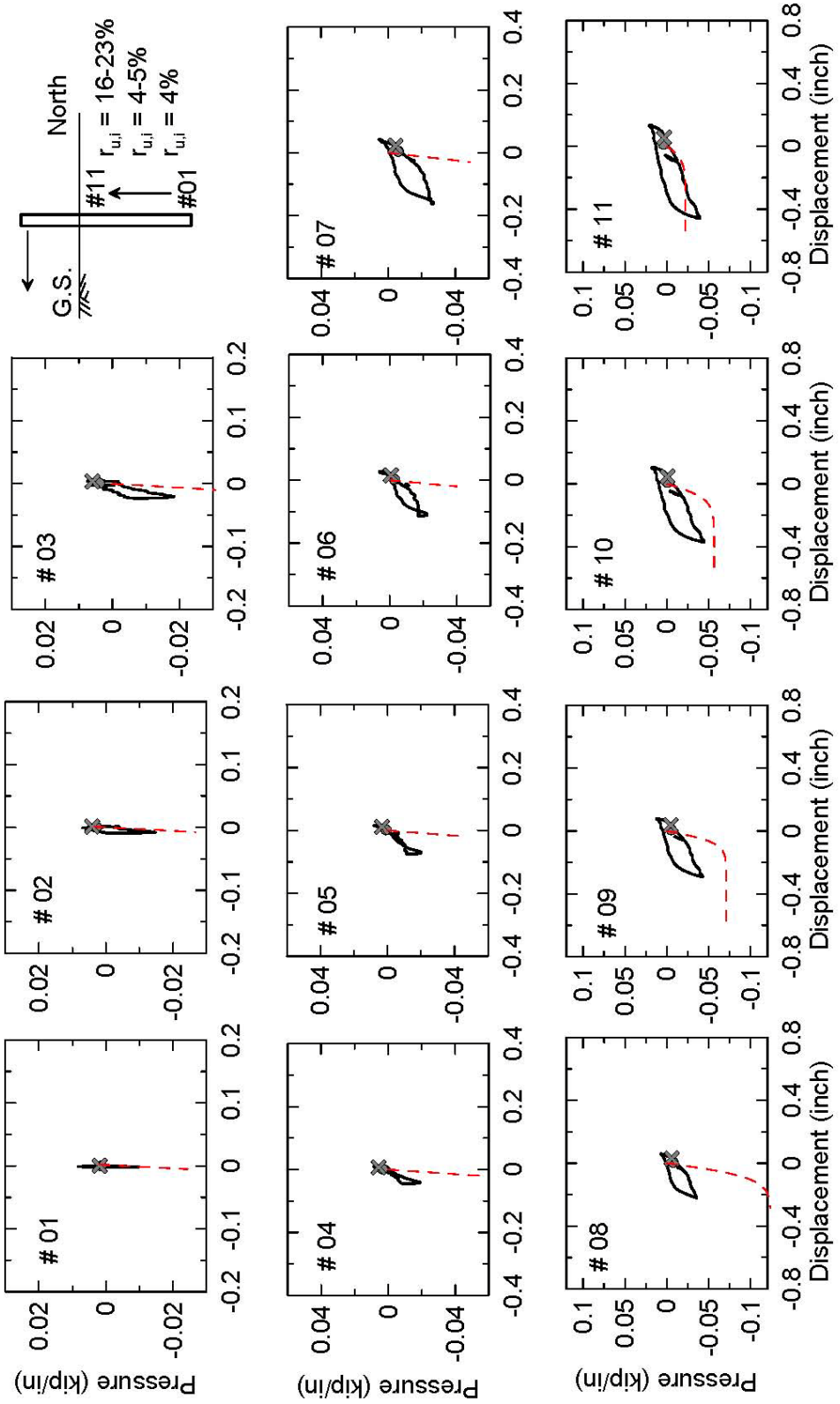

Figure 3-29: Circle denotes beginning of test; "x" denotes end of test. Dashed red line denotes bilinear API p-y curve

Figure 3-30. P-y curves for static C

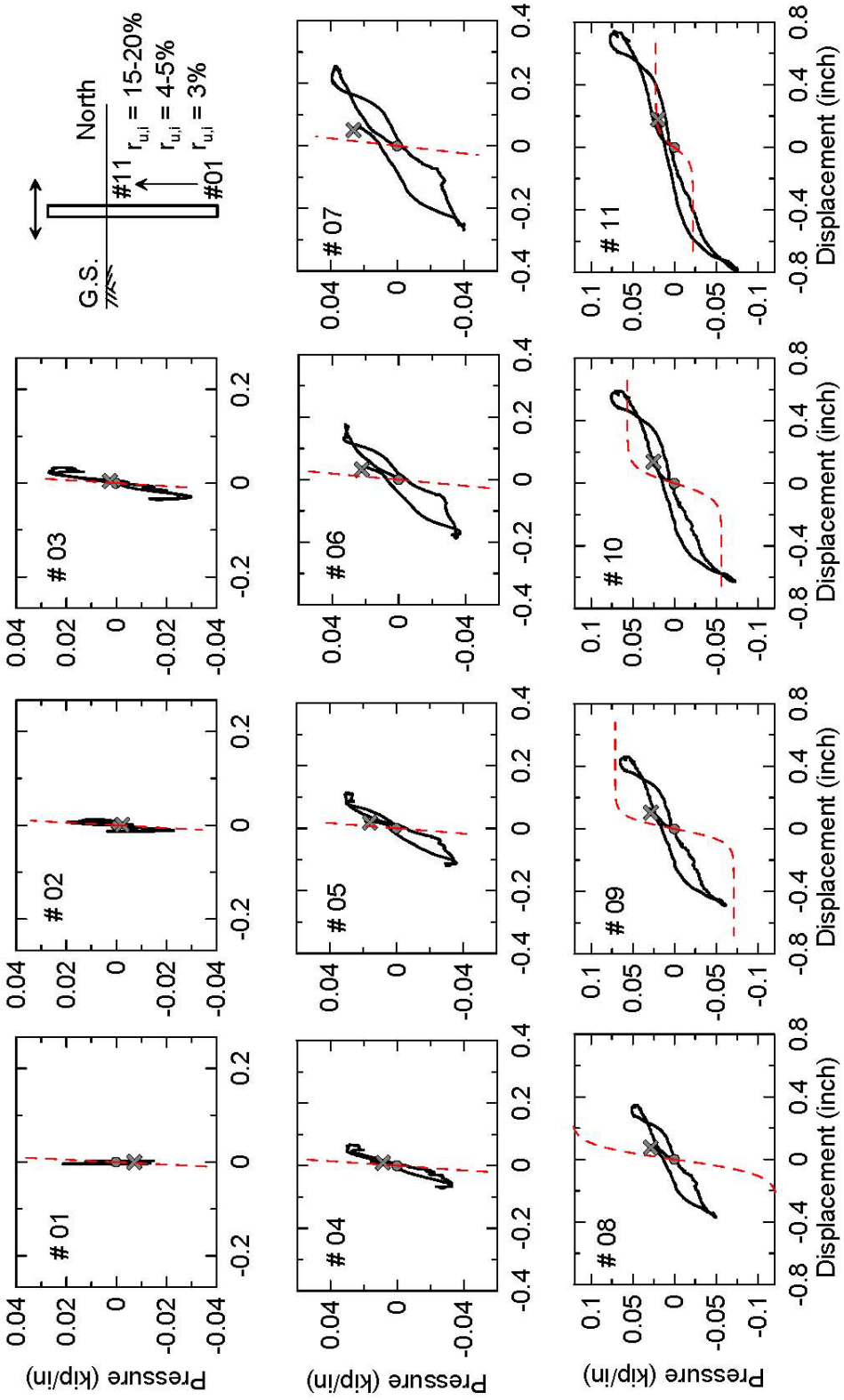

Figure 3-30: Circle denotes beginning of test; "x" denotes end of test. Dashed red line denotes bilinear API p-y curve

Figure 3-31. Comparison of p-y curves for static tests A, B, and C

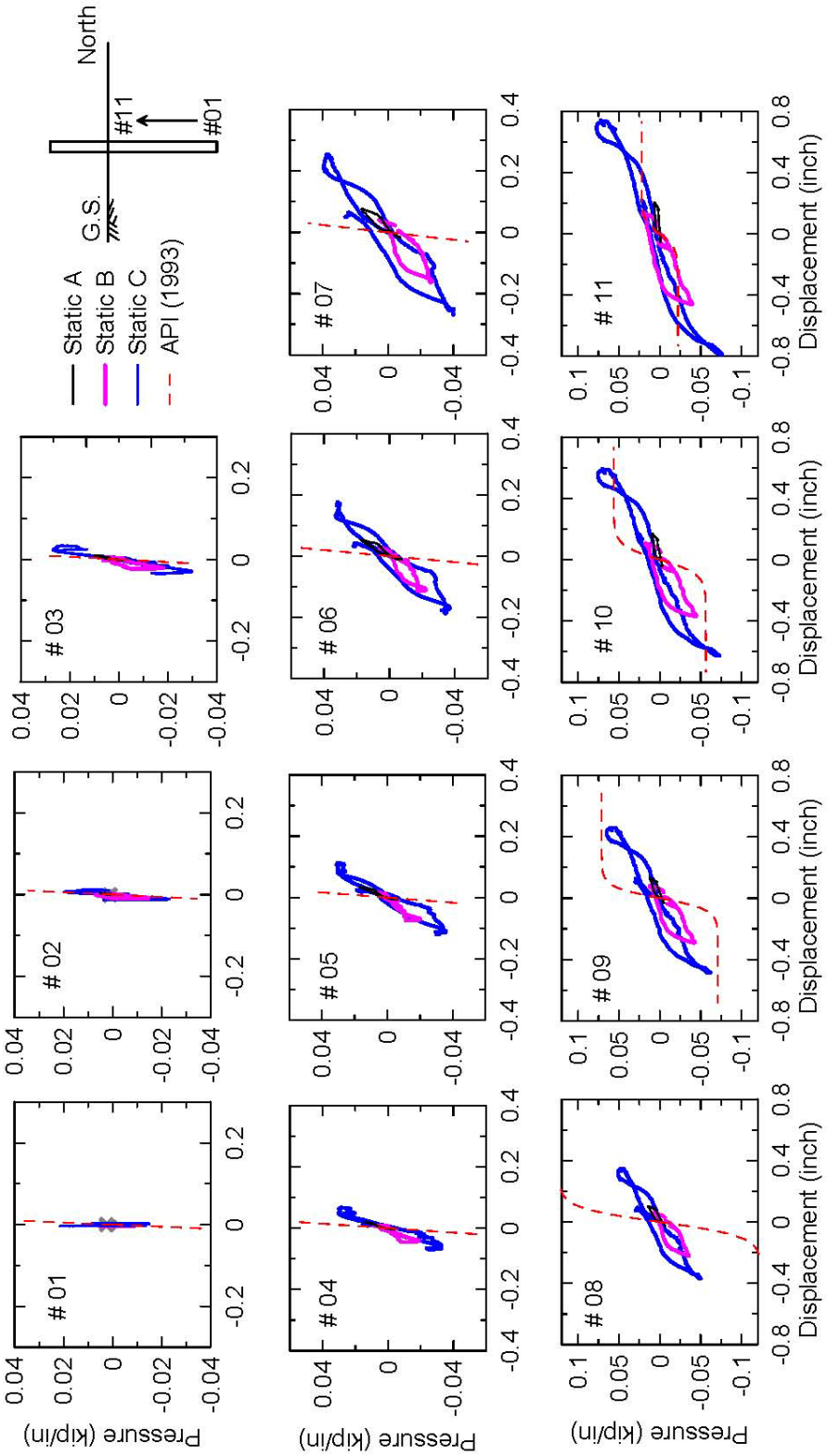

Figure 3-31: Dashed red line denotes bilinear API p-y curve.

Figure 3-32. Close-up comparison of p-y curves for static tests A, B, and C

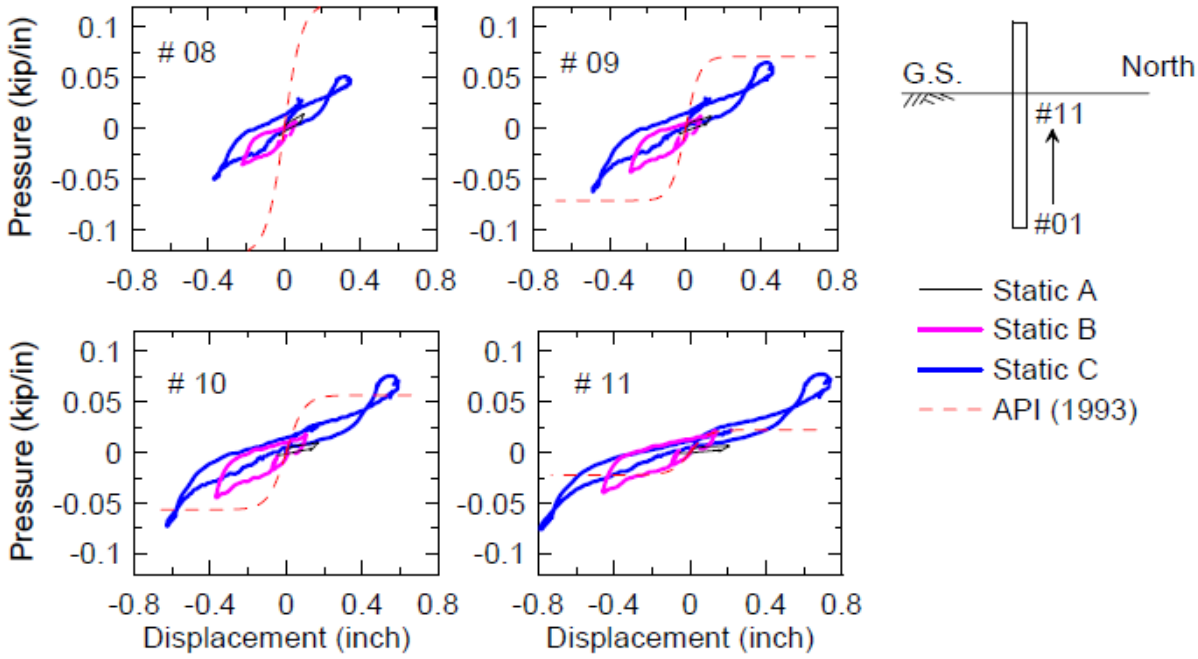

Figure 3-32: Dashed line denotes bilinear API p-y curve.

4. Concluding Remarks

This report presents details of the design and construction of a single pile specimen surrounded by loose saturated sand and an associated test protocol involving sequential testing of the model first under low amplitude base shaking sinusoidal waves and subsequently under inertial loading of the pile head. Test results are presented to document the construction and dynamic pore pressures of the model as well as the static load-displacement behavior of the soil-pile system and bending moment distributions in the pile. Back-calculated p-y curves at various levels of excess pore pressure are presented.

A rich set of test data was produced from this testing series. Analyses of test results indicate that lateral loading was conducted while excess pore pressures were elevated post-shake. Subsequently, mobilization of the partially liquefied soil was achieved during lateral loading. Additional data which was evaluated include wave test measurements (hammer strikes to model), settlement and acceleration measurements. Results focus in particular on the static p-y curves extracted from the bending moment distributions at the achieved excess pore pressures. These data should be useful for calibration of numerical modeling of soil-pile systems for use in designs.

This page left blank intentionally.

Appendix A
GeoCon Soils Testing Report

This page left blank intentionally.

Figure A.1: GeoCon Soils Report.

GeoTesting express
A subsidiary of Geocomp Corporation

Client:	Shannon & Wilson				
Project:	Columbia River Crossing				
Location:	Washington / Oregon			Project No:	GTX-9076
Boring ID: ---		Sample Type:	bag	Tested By:	mmd
Sample ID:	Nevada Sand	Test Date:	06/08/09	Checked By:	mpd
Depth :	---	Test Id:	154048		
Test Comment:	Hydrometer not required, less than 10% fines.				
Sample Description:	Dry, pinkish white sand				
Sample Comment:	---				

Particle Size Analysis - ASTM D 422-63 (reapproved 2002)

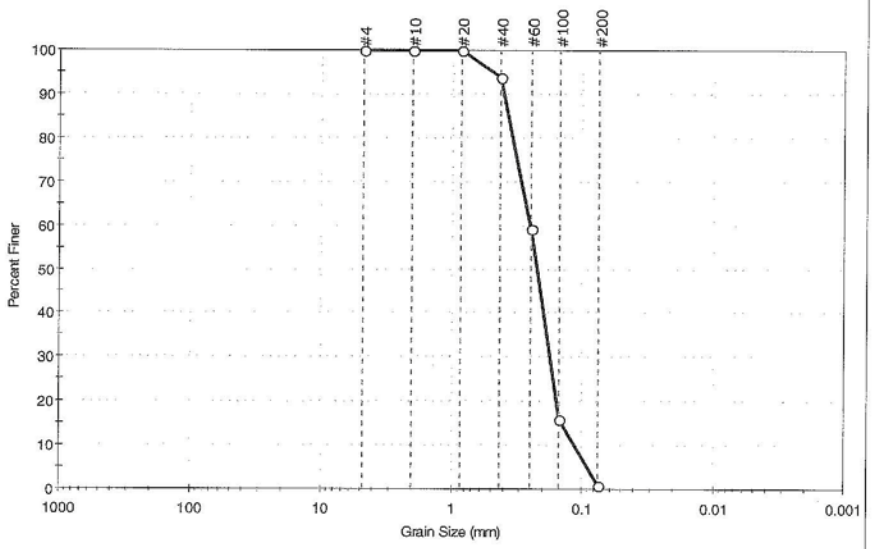

%Cobble	%Gravel	%Sand	%Silt & Clay Size
---	0.0	99.0	1.0

Sieve Name	Sieve Size, mm	Percent Finer	Spec. Percent	Complies
#4	4.75	100		
#10	2.00	100		
#20	0.85	100		
#40	0.42	94		
#60	0.25	59		
#100	0.15	16		
#200	0.075	1		

Coefficients

D_{85} =0.3706 mm	D_{30} =0.1771 mm
D_{60} =0.2524 mm	D_{15} =0.1444 mm
D_{50} =0.2239 mm	D_{10} =0.1143 mm
C_U =2.208	C_C =1.087

Classification

ASTM Poorly graded sand (SP)

AASHTO Fine Sand (A-3 (0))

Sample/Test Description

Sand/Gravel Particle Shape : ---

Sand/Gravel Hardness : ---

printed 6/11/2009 4:38:41 PM

This page left blank intentionally.

Figure A.2: GeoCon Soils Report.

GeoTesting express
a subsidiary of Geocomp Corporation

Client:	Shannon & Wilson				
Project:	Columbia River Crossing				
Location:	Washington / Oregon			Project No:	GTX-9076
Boring ID: ---		Sample Type:	bag	Tested By:	ap
Sample ID:	Nevada Sand	Test Date:	06/11/09	Checked By:	mpd
Depth :	---	Test Id:	154049		
Test Comment:	---				
Sample Description:	Dry, pinkish white sand				
Sample Comment:	---				

Specific Gravity of Soils by ASTM D 854-06

Boring ID	Sample ID	Depth	Visual Description	Specific Gravity
---	Nevada Sand	---	Dry, pinkish white sand	2.64

Notes: Specific Gravity performed by using method A (oven dried specimens) of ASTM D 854
Moisture Content determined by ASTM D 2216.

printed 6/11/2009 4:20:36 PM

This page left blank intentionally.

Figure A.3: GeoCon Soils Report.

GeoTesting express
a subsidiary of Geocomp Corporation

Client:	Shannon & Wilson	Test Date:	06/09/09
Project Name:	Columbia River Crossing	Tested By:	saa
Project Location:	WA/OR	Checked By:	mpd
GTX #:	9076		

Minimum Density of Soil by ASTM D 4254 and Maxium Density of Soil Using a Vibratory Table by ASTM D 4253

Boring ID	Sample ID	Depth, ft	Visual Description	Minimum Density, lb/ft³	Void Ratio at Minimum Density	Maximum Density, lb/ft³	Void Ratio at Maximum Density
---	Nevada Sand	---	Dry, pinkish white sand	97.27	0.690	110.03	0.494

Notes: Minimum density determined on a dry sample using Method A using a 0.100 cuft mold
Maximum density determined on a dry sample using Method 1A using a 0.100 cuft mold
The double amplitude of vertical vibration was the standard 0.013 ± 0.002 in.

This page left blank intentionally.

Appendix B
Instrument Sensitivity

This page left blank intentionally.

Table B.1: Instrument Sensitivity.

Instrument type	Instrument name	Units	Sensitivity	Max. range
Strain gage	SGN01 -SGN15 SGS01 -SGS15	$\mu\in$	± 10	30,000
Pore pressure transducer	PP1 -PP5	psi	± 0.008	29.009
Soil pressure transducer	SP01 -SP10	psi	± 0.02	29.01
Accelerometer	A01 -A17	g	0.002	± 2 or ± 4 (varies)
Inclinometer	I01 -I02	degrees	± 0.030	45
String potentiometer	D1 -D8	inch	0.013” to 0.024”	15” to 50” (varies) (total stroke)
Linear potentiometer	Vsettle	inch	± 0.0006”	12” (total stroke)

This page left blank intentionally.

Appendix C
Bibliography

This page left blank intentionally.

Table C.1: Bibliography.

API (1993). "Recommended practice for planning, designing and constructing fixed offshore platforms." 20th edition RP 2A-WSD, American Petroleum Institute.

Ashford, S. and Jakrapiyanun, W. (2001). "Design and verification of the UCSD laminar container." SSRP 2001-07, University of California, San Diego.

Baldi, G., Bellotti, R., Ghionna, V., Jamiolkowsky, M., and Lo Presti, D. (1989). "Modulus of sands from cpt's and dmt's." Proceedings, 12th International Conference on Soil Mechanics and Foundation Engineering, Rio de Janeiro, Brazil(Vol 1), 160–170.

Bartake, P. and Singh, D. (2007). "Studies on the determination of shear wave velocity in sands." Geomechanics and Geoengineering: An International Journal, 2(1), 41–49.

Berezin, I. and Zhidkov, N. (1965). Computing Methods, Volume I. Addison-Wesley Publishing Company.

Bowles, J. (1996). Foundation Analysis and Design. The McGraw-Hill Companies.

Brandenberg, S. (2005). "Behavior of pile foundations in liquefied and laterally spreading ground," PhD thesis, University of California, Davis.

Brandenberg, S., Boulanger, R., Kutter, B., and Chang, D. (2005). "Behavior of pile foundations in laterally spreading ground during centrifuge tests." Journal of Geotechnical and Geoenvironmental Engineering, 131(11), 1378–1391.

Burden, R. and Faires, J. (1993). Numerical Analysis. PWS Publishing Company.

Day, R. (2000). Geotechnical Engineer's Portable Handbook. McGraw Hill.

Feagin, L. (1937). "Lateral pile-loading tests." Transactions of ASCE, Paper #1959, 102, 236–254.

Holtz, R. and Kovacs, W. (1981). An Introduction to Geotechnical Engineering. Prentice Hall, Upper Saddle River, New Jersey.

Idriss, I. and Boulanger, R. (2008). Soil Liquefaction during Earthquakes. Earthquake Engineering Research Institute.

Kramer, S. (1996). Geotechnical Earthquake Engineering. Prentice Hall.

Kulhawy, F. and Mayne, P. (1990). "Manual on estimating soil properties for foundation design." Electric Power Institute, Palo Alto, California.

Lee, K., Shen, C., Leung, D., and Mitchell, J. (1999). "Effects of placement method on geotechnical behavior of hydraulic fill sands." Journal of Geotechnical and Geoenvironmental Engineering, 125(10), 832–846.

Liu, L. and Dobry, R. (January 1995). “Effect of liquefaction on lateral response of piles by centrifuge model tests.” National Center for Earthquake Engineering Research (NCEER) Bulletin, 9(1), 7–11.

Matlock, H. (1970). “Correlations for design of laterally loaded piles in soft clay.”

Second Annual Offshore Technology Conference, Houston, Texas, Paper Number 1204.

Matthews, J. (1982). “Shear wave velocity measurements in marine sediments.” Geo-Marine Letters, 2, 215–217.

Meymand, P. (1998). “Shaking table scale model tests of nonlinear soil-pile-superstructure interaction in a soft clay,” PhD thesis, University of California, Berkeley.

Reese, L., Cox, W., and Koop, F. (1974). “Analysis of laterally loaded piles in sand.” Sixth Annual Offshore Technology Conference, Houston, Texas, Paper Number 2080.

Reese, L., Wang, S., Isenhower, W., Arrellaga, J., and Hendrix, J. (2000). LPILE. Ensoft, Inc.

Rollins, K., Bowels, S., Brown, D., and Ashford, S. (June 25-28, 2007). “Lateral load testing of large drilled shafts after blast-induced liquefaction.” 4th International Conference on Earthquake Engineering, Thessaloniki, Greece, (1141).

Rollins, K., Gerber, T., Lane, J., and Ashford, S. (2005). “Lateral resistance of a full-scale pile group in liquefied sand.” Journal of Geotechnical and Geoenvironmental Engineering, 131(1), 115–125.

Rollins, K., Hales, L., Ashford, S., and Camp, W. (2005). “P-y curves for large diameter shafts in liquefied sand from blast liquefaction tests.” ASCE Special Publication No. 145: Seismic Performance and Simulation of Pile Foundations in Liquefied and Laterally Spreading Ground, 11–23.

Salgado, R. (2008). The Engineering of Foundations. McGraw-Hill Companies, New York, New York.

Salgado, R., Mitchell, J., and Jamiolkowski, M. (1997). “Cavity expansion and penetration resistance in sand.” Journal of Geotechnical and Geoenvironmental Engineering, 123(4), 344–354.

Salgado, R. and Prezzi, M. (2007). “Computation of cavity expansion pressure and penetration resistance in sands.” International Journal of Geomechanics, 7(4), 251– 265.

Seed, H. and Idriss, I. (1970). “Soil moduli and damping factors for dynamic response analyses.” Report EERC 70-10, Earthquake Engineering Research Center (University of California, Berkeley).

Tokimatsu, K. and Suzuki, H. (2004). “Pore water pressure response around pile and its effects on p-y behavior during soil liquefaction.” Soils and Foundations, 44(6), 101–110.

Tokimatsu, K., Suzuki, H., and Suzuki, Y. (2001). “Back-calculated p-y relation of liquefied soils from large shaking table tests.” Fourth International Conference on Recent Advances in Geotechnical Earthquake Engineering and Soil Dynamics.

Weaver, T. (2001). “Behavior of liquefying sand and CISS piles during full-scale lateral load tests,” PhD thesis, University of California, San Diego.

Weaver, T., Ashford, S., and Rollins, K. (2005). “Response of 0.6 m cast-in-steel-shell pile in liquefied soil under lateral loading.” Journal of Geotechnical and Geoenvironmental Engineering, 131(1), 94–102.

Wilson, D. (1998). “Soil-pile-superstructure interaction in liquefying sand and soft clay,” PhD thesis, University of California, Davis.

Wilson, D., Boulanger, R., and Kutter, B. (2000). “Observed seismic lateral resistance of liquefying sand.” Journal of Geotechnical and Geoenvironmental Engineering, 126(10), 898–906.

Yang, J. (2002). “Liquefaction resistance of sand in relation to p-wave velocity.” Geotechnique, 52(4), 295–298.

Yang, J. and Sato, Y. (2000). “Interpretation of seismic vertical amplification observed at an array site.” Bulletin of the Seismological Society of America, 90(2), 275–285.

This page left blank intentionally.